MATERIALS CHEMISTRY
FRONTIERS

RESEARCH ARTICLE

View Article Online
View Journal | View Issue



Cite this: *Mater. Chem. Front.*, 2025, **9**, 866

# Arrays of ultra-thin selenium-doped zirconium-anodic-oxide nanorods as potential antibacterial coatings†

Kirill Kamnev, [a] Maria Bendova, [ab] Zdenka Fohlerova, [b] Tatiana Fialova, [c] Oleh Martyniuk, [a] Jan Prasek, [ab] Kristyna Cihalova [c] and Alexander Mozalev *[ab]

Two characteristic types of extraordinarily thin upright-standing $ZrO_2$-based nanorods self-aligned on a substrate, differing in diameters (20/30 nm), lengths (90/120 nm), and population densities (1.1/4.6 × $10^{10}$ $cm^{-2}$), were synthesized *via* the porous-anodic-alumina (PAA)-assisted anodization of Zr in 1.5 M selenic acid followed by selective PAA dissolution. A needle-like shape was achieved due to the unique formation of zirconium anodic oxide in extremely thin nanopores that grow only in selenic acid. The SEM, XPS, and Raman spectroscopy analyses revealed that the nanorods feature a core/shell structure in which the core is stoichiometric amorphous $ZrO_2$, and the shell is ~6 nm thick hydroxylated zirconium dioxide $ZrO_{2-x}(OH)_{2x}$ mixed with $Al_2O_3$. The core and shell incorporated electrolyte-derived selenate ($SeO_4^{2-}$) ions, which replace up to 1% of the $O^{2-}$ ions in the nanorod surface layer. Besides, nanoparticles of elemental Se were deposited on the top of rods during anodic polarization. A model was developed for the cooperative ionic transport and electrochemical and solid-state reactions during the PAA-assisted growth of zirconium oxide in selenic acid. The two Se-doped top-decorated zirconium-oxide nanorod arrays were examined as potential antibacterial nanomaterials toward G-negative *E. coli* and G-positive *S. aureus*, using direct SEM observations of the bacteria–surface interfaces and carrying out the modified Japanese Industrial Standard test for antimicrobial activity and efficacy, JIS Z 2801. While specific differences in interaction with each type of bacteria were observed, both nanostructures caused a significant harmful synergetic effect on the bacteria, acting as non-metallic (Se) ion-releasing bactericidal coatings along with repellent and contact-killing activities arising from extraordinary needle-like nanoscale surface engineering.

Received 10th December 2024,
Accepted 16th January 2025

DOI: 10.1039/d4qm01081g

rsc.li/frontiers-materials



## Introduction

Zirconium-oxide-based ceramic and composite materials have been produced and utilized in surface protection, sensing, filtering, electronics, catalytic, and biomedical applications.[1–7] The reported $ZrO_2$ fabrication methods include chemical spray pyrolysis, physical vapor deposition, sol–gel, hydrothermal synthesis, pulsed laser deposition, and electrochemical conversion.[8–12] Electrochemical conversion is especially attractive due to the low cost, scalability, and simplicity of the approach utilizing electrode reactions combined with the electric field-driven zirconium- and oxygen-ion migration to form $ZrO_2$ coatings on the Zr metal. Thin continuous featureless or self-ordered micro- and nanostructured $ZrO_2$ coatings can be electrochemically synthesized in a highly reproducible manner required for state-of-the-art $ZrO_2$ applications.[1,3,6]

Typical electrochemical conversion approaches for $ZrO_2$ fabrication include barrier-type anodization, plasma electrolytic oxidation (PEO), and nanoporous (nanotubular) anodization.[12–15] Barrier-type anodization generates conformal microscopically flat submicrometer-thick $ZrO_2$ layers on the zirconium metal. PEO converts the zirconium surface into a micrometer- to millimeter-thick $ZrO_2$ coating comprising randomly distributed micro-scale pores and cracks. Nanotubular anodization generates $ZrO_2$ nanotubes of thicknesses up to tens of micrometers. In addition, a novel alternative method has recently been developed to

[a] *CEITEC – Central European Institute of Technology, Brno University of Technology, Purkynova 123, 61200 Brno, Czech Republic*
[b] *Department of Microelectronics, Faculty of Electrical Engineering and Communication, Brno University of Technology, Technicka 10, 61600 Brno, Czech Republic. E-mail: mozalev@vutbr.cz*
[c] *Department of Chemistry and Biochemistry, Mendel University in Brno, Zemedelska 1, 61300 Brno, Czech Republic*

† Electronic supplementary information (ESI) available: XPS spectra and their analysis and SEM observation of bio-interfaces. See DOI: https://doi.org/10.1039/d4qm01081g

 

synthesize self-organized $ZrO_2$-based nanostructures such as dots, columns, or rods self-arrayed on a substrate.[16–18] The method involves anodizing a thin Al layer superimposed on the Zr layer (Al/Zr bilayer) to convert the upper aluminum into a porous anodic alumina (PAA) film and subsequently transform the zirconium underlayer into its anodic oxide locally through the PAA nanopores – PAA-assisted anodization. Selective chemical dissolution of the PAA overlayer yields an array of $ZrO_2$ nanocolumns or nanorods spatially separated from each other and upright standing either on a buffering zirconium-oxide underlayer[17] or directly on the remaining zirconium metal.[16]

A unique nanorod morphology of $ZrO_2$ coatings produced by PAA-assisted anodization is advantageous for applications requiring a substantially enlarged surface-to-volume ratio and high permeability.[1,3,6] Unlike nanotubular $ZrO_2$ surfaces, nanorod arrays provide higher freedom in modulating the surface response toward external factors such as water, oils, or living cells.[19,20] The geometrical parameters of the PAA-assisted $ZrO_2$ nanorods, the center-to-center distance, diameter, height, and population density, can be tailored or tuned by simply adjusting the formation conditions. Various morphologies of the PAA-assisted $ZrO_2$ nanostructures have revealed dissimilar impacts on the lifecycle of human osteoblasts, which were able to differentiate between the geometries and surface arrangements of oxide nanostructures.[20] The nature of the anodizing electrolyte not only determines the nanostructures' dimensions but also significantly alters their chemical composition *via* incorporating various electrolyte-derived species. Such impurities may reportedly impact the metabolism and lifecycle of adhered cells.[20,21]

Selenic-acid aqueous solution or ''selenic acid'' is a novel anodizing electrolyte unique for growing PAA with the narrowest nanopores and the lowest porosity.[22,23] In our recent work, the growth of slender $Nb_2O_5$ nanostructures was achieved *via* the PAA-assisted anodization of niobium in the selenic-acid electrolyte.[24] The PAA-assisted anodization of zirconium in selenic acid is anticipated to generate similarly thin $ZrO_2$ nanostructures, resembling the surface morphology of cicada wings, which have been the subject of investigation because of their antibacterial properties.[25] The ultra-thin $ZrO_2$ nanorods could modulate the surface response to microbial pathogens *via* similar mechanisms of cell membrane piercing, adhesion-induced rupture, and oxidative stress generation.[25] Furthermore, selenic species may be incorporated into the $ZrO_2$ nanorods simply during the anodization in selenic acid. Since selenium and its compounds have revealed antioncogenic and bactericidal properties,[26,27] selenium-doped $ZrO_2$ surfaces could also function as non-metallic-ion-releasing antibacterial coatings.[28] This feature, in addition to the mechano-penetration, may further boost the antibacterial response of $ZrO_2$ nanorods by promoting the synthesis of reactive oxygen species (ROS) in bacteria and facilitating cell lysis.[29]

In the present work, $ZrO_2$ nanostructured coatings were synthesized *via* the PAA-assisted anodization of zirconium in a selenic-acid aqueous solution under various formation conditions to accomplish the self-organized growth of several distinctive types of $ZrO_2$ nanostructures within the super-narrow PAA nanopores that cannot be achieved in any other anodizing solution. The films' morphology, structure, and chemical composition were examined by scanning electron microscopy (SEM), Raman spectroscopy, and X-ray photoelectron spectroscopy (XPS) to disclose the mechanism for the PAA-assisted growth of $ZrO_2$ nanostructures in the selenic acid. For assessing the bactericidal properties of the novel arrays, the interaction of the developed surfaces with Gram-negative *Escherichia coli* (*E. coli*) and Gram-positive *Staphylococcus aureus* (*S. aureus*) bacteria was studied by direct high-resolution SEM observation of the films/bacteria interfaces and evaluating the surfaces' antibacterial activity by the modified JIS Z 2801 test assay.

## Experimental part

### Sample preparation

A 150 nm thick layer of zirconium followed by either a 300 nm thick or a 550-nm thick layer of aluminum (Al/Zr bilayer) were sequentially deposited by DC magnetron sputtering onto polished nanoscopically flat 4″ $SiO_2$-coated Si wafers. The magnetron sputtering was carried out using Zr (99.95%) and Al (99.999%) targets. The wafers with the deposited Al/Zr metal bilayers were cut into *ca.* 1.4 cm × 1.4 cm pieces and anodized individually in a custom-made polytetrafluoroethylene two-electrode cell with a $\sim$0.8 $cm^2$ (1.0 cm in diameter) circular working area. An aqueous solution of 1.5 M $H_2SeO_4$ (Merck & Co, USA) was used as the anodizing electrolyte. Anodization was carried out at 23 °C in a combined potentiodynamic–potentiostatic regime: first, the Al/Zr bilayers were processed using potentiodynamic polarization with a voltage sweep rate of 0.35 V $s^{-1}$ up to 22 or 45 V, followed by a 90-second potentiostatic polarization in both cases. Selected samples were re-anodized (anodized again to a higher voltage) in the same electrolyte using potentiodynamic polarization with a substantially faster voltage sweep rate of 10 V $s^{-1}$ up to either 80 or 120 V, followed again by a 60-second potentiostatic polarization to ensure a uniform anodic oxide formation across the entire sample surface.

The anodized and re-anodized samples were thoroughly rinsed with Milli-Q® ultrapure water and dried in a cool nitrogen stream. Then, the samples were dipped in 0.2 M $CrO_3$ and 0.45 M $H_3PO_4$ solution at 65 °C for 45 minutes to dissolve the PAA overlayer[30] (hereafter the 'selective etchant'), rinsed with ultrapure water, and dried in a cool nitrogen stream.

Furthermore, two types of flat $ZrO_2$ anodic films were prepared for comparison with the nanostructured anodic oxides: a 150 nm thick Zr film was magnetron sputter-deposited onto a $SiO_2$-coated Si wafer. Individual pieces of *ca.* 1.5 cm × 1.5 cm cut from this wafer were anodized in (1) 1.5 M $H_2SeO_4$ and (2) 0.1 M $H_3PO_4$ aqueous solutions by potentiodynamic polarization up to 20 V with a rate of 0.1 V $s^{-1}$, followed by a 5-min potential hold. In both cases, compact microscopically flat anodic oxides, about 50 nm thick, were grown on the

zirconium surfaces. The selenic-acid-anodized $ZrO_2$ film was expected to have incorporated electrolyte-derived Se species, while the phosphoric-acid-anodized film was supposed to be Se-free $ZrO_2$.

### Sample analysis

The morphology of the anodic films was analyzed using an FEI Verios 460L field-emission SEM operating in immersion mode at an accelerating voltage of 15 kV and a probe current of 0.8 nA. After conducting biological tests, the surfaces and cross-sections of the anodic films were observed using a TESCAN MIRA II SEM operated at an accelerating voltage of 15 or 30 kV, depending on the bacteria/substrate interfaces. The images were analyzed using ImageJ software.

The films' structure and composition were examined by Raman spectroscopy using a confocal Raman microscope WITec Alpha300 R+. All measurements were performed using a 532 nm excitation laser source with power reduced to 1 mW and focused using a 100× objective (NA 0.9, WD 0.31 mm). Individual spectra were recorded with over 1800 accumulations and a 2 s integration time (a total of 60 min exposure time).

The chemical composition and bonding states at the film surfaces were analyzed by XPS using a Kratos Axis Supra spectrometer employing a monochromatic Al Kα source (X-ray emission power 225 W). Typical operating pressures were less than $1.3 \times 10^{-9}$ mbar. For the survey and high-resolution spectra, the emitted electrons were detected at fixed pass energies of 160 and 20 eV, respectively. A Kratos charge neutralizer system was employed for all measurements. The CasaXPS software version 2.3.17 was used for spectra analysis.[31] The spectra were charge corrected to give the adventitious C 1s spectral component (C–C and C–H) binding energy of 285.0 eV. The deconvolution of C 1s narrow scans was performed as described in previous works,[31–34] with more details available in the ESI.† The quantitative evaluation was accomplished from the narrow spectra using the relative sensitivity factors from CasaXPS (referenced to F 1s) suitable for the Kratos Axis spectrometer.

### Antibacterial activity

Two bacterial strains from the Czech Collection of Microorganisms, *E. coli* CCM 3954 and *S. aureus* CCM 4223, were used to assess the antibacterial properties of synthesized coatings. The film-surface/bacteria interfaces were observed by SEM. Selected samples were immersed in 2 mL of the bacterial inoculum in Brain Heart Infusion Agar (Merck & Co., USA) and incubated at 37 °C for 5 h. After incubation, samples were gently washed with phosphate-buffered saline (PBS) (Merck & Co., USA). The surface-adhered bacteria were fixated in 2 wt% glutaraldehyde for 1 h. The samples were dehydrated by rinsing for 15 min in aqueous solutions with graded ethanol concentrations (once in 30, 50, 70, 80, 90, and 95 and twice in 100 wt%) and directly observed using an electron microscope without depositing any conducting material.

The surface antibacterial activity was measured following the modified Japanese Industrial Standard test for antimicrobial activity and efficacy JIS Z 2801. After overnight cultivation on Columbia blood agar (Labmediaservis, Czech Republic), *E. coli* CCM 3954 and *S. aureus* CCM 4223 bacterial strains were diluted in a liquid medium to make a bacterial inoculum with concentrations of 1.6 and $1.2 \times 10^{11}$ colony-forming units (CFU) per 1 mL, respectively, determined by optical density measurements at 600 nm. Following a brief sample disinfection by UV light, 100 μL of the bacterial inoculum in Mueller–Hinton broth (Merck & Co., USA) was applied over the active surface of each sample ($<0.8$ cm$^2$). A borosilicate glass slide sterilized by washing in ethanol and exposing it to UV light was used as the objective control in the experiment. All samples were incubated at 37 °C and 90% humidity for 24 h. Then, the surface was thoroughly washed with PBS solution to remove all bacteria. After serial decimal dilution, saline with bacteria was inoculated on Mueller–Hinton agar Petri dishes (Merck & Co., USA) at 37 °C for 24 h, and the number of bacterial colonies was calculated and expressed in CFU cm$^{-2}$.

## Results and discussion

### Part I: Anodic oxide growth

**Anodizing behavior.** The individual Al(300 nm)/Zr(150 nm) and Al(550 nm)/Zr(150 nm) bilayer samples were anodized in 1.5 M $H_2SeO_4$ at two distinct anodizing voltages $U_a$ = 22 and 45 V and then re-anodized to $U_r$ = 80 and 120 V, respectively. The voltage–time and current–time responses during the anodization and re-anodization are shown in Fig. 1. The 550 nm thick Al layer was needed to proceed with the 45 V anodization because the 300 nm Al layer was insufficiently thick for establishing a steady-state regime of pore growth.

The anodic processes are divided into three characteristic stages, as depicted in the insets in Fig. 1. A self-ordered PAA film grows at Stage I. Stage II begins when the PAA barrier layer touches the Zr underlayer, and anodizing the Zr metal commences through the PAA nanopores. The re-anodization to a higher voltage at Stage III makes rapidly growing $ZrO_2$ partially fill the PAA pores and simultaneously create a buffering oxide layer under the pores.

Samples anodized to the end of Stages II will be hereafter referred to as the 22 V and 45 V samples, respectively. Samples re-anodized till the end of Stage III will be named the 22–80 V and 45–120 V samples, as pointed out in Fig. 1.

**Oxide morphology.** The surfaces and cross-sections were observed after selectively dissolving the PAA overlayer, as described elsewhere.[35] It was revealed that the electrical conditions employed for anodizing and re-anodizing the Al/Zr bilayer have a pronounced impact on the surface morphology. From the SEM views in Fig. 2a, the surface of the 22 V sample is populated with protrusions having a center-to-center distance $D_{cent}$ of 50 nm. From the cross-sectional view in Fig. 2b, the protrusions of the 22 V sample resemble nanocones with spread-out bases and slim apexes. Each cone is ∼20 nm tall and resides on a ∼10 nm thick compact bottom-oxide layer having a concave-like profile at the oxide/metal interface. The re-anodized

 

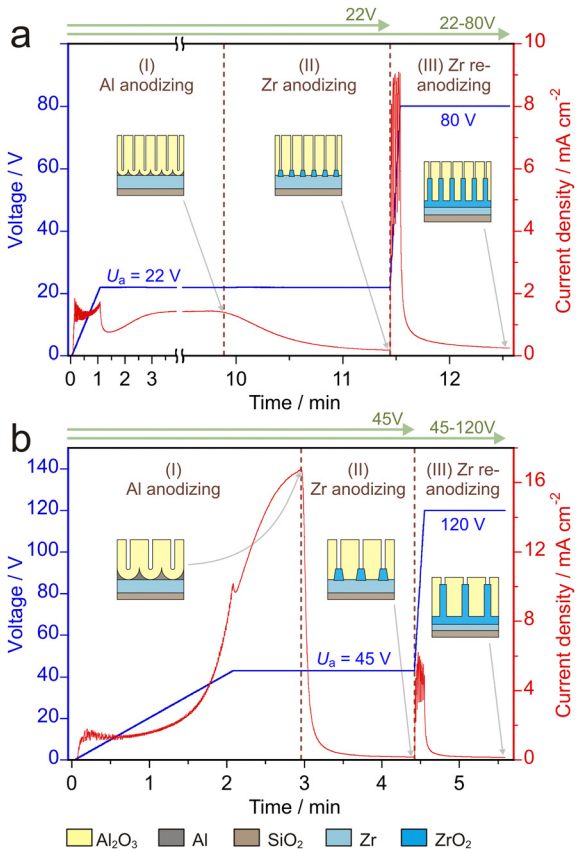


Fig. 1 Voltage–time and current–time responses during anodization and re-anodization of (a) an Al(300 nm)/Zr(150 nm) bilayer and (b) an Al(550 nm)/Zr(150 nm) bilayer in the 1.5 M $H_2SeO_4$ electrolyte at 23 °C for forming two types of $ZrO_2$ nanostructures with different sizes and geometries. Stage I: potentiodynamic Al anodization with a sweep rate of 0.35 V s$^{-1}$ up to an anodizing voltage of $U_a$ = (a) 22 V or (b) 45 V. Stage II: potentiostatic Zr anodization at (a) 22 V or (b) 45 V. Stage III: Potentiodynamic Zr re-anodization with a sweep rate of 10 V s$^{-1}$ up to (a) 80 or (b) 120 V, followed by a potential hold. As specified above in the plots, the samples are named according to anodizing voltages (22 V and 45 V) – Stage II and the re-anodizing voltages (22–80 V and 45–120 V) – Stage III. The embedded schematics show how the films are anticipated to develop at the end of the corresponding stages.

22–80 V sample (Fig. 2c and d) is populated with thin needle-like nanorods, 20 nm in diameter and 90 nm tall, distanced by the same $D_{cent}$ = 50 nm. The nanorods are anchored to a 50-nm thick compact bottom oxide layer, buffering the rods from the remaining Zr metal.

The nanocones of the 45 V sample (Fig. 3a and b) are 55 nm tall, separated by $D_{cent}$ = 103 nm (mean value), and buffered from the Zr metal by a 10–20 nm thick bottom-oxide layer. In the re-anodized 45–120 V sample, the cones transform to 120 nm tall nanorods, 30 nm in diameter, separated by the same $D_{cent}$ = 103 nm (Fig. 3c and d) and anchored to a 50 nm thick continuous bottom-oxide layer. One may see that the tips of the rods are thinner than the rods' bodies (insets in Fig. 2d and 3d). The shape of the tips may, to an extent, be controlled by varying the voltage sweep rate (current density) and the length of the voltage hold at Stage III (Fig. 1): the slower the sweep rate and the longer the potential hold, the flatter the tips. For the purpose of the present study, we have chosen very fast re-anodization followed by a short voltage hold to make the tips of the rods 'sharper'.

For qualitatively differentiating the samples by their sizes and type of morphology, the 22 V and 45 V anodized samples will be nicknamed, respectively, the "small nanocones" and "big nanocones", while the 22–80 V and 45–120 V samples will be the "small nanorods" and "big nanorods", respectively. The relationships between the sample formation conditions and their geometrical features are summarized in Table 1.

**Control over surface morphology.** The PAA-assisted zirconium anodization in 1.5 M $H_2SeO_4$ produces nanostructured $ZrO_2$ coatings with highly controllable nanoscale features (Fig. 2 and 3) quantitatively related to anodizing variables. The interpore distance ($D_{int}$) in a PAA film is known to depend on $U_a$ through a proportionality constant $k$:[36]

$$D_{int} = k \cdot U_a \quad (1)$$

The PAA-assisted $ZrO_2$ nanostructures fully match the pore distribution in the upper PAA layer;[18,24] therefore, $D_{int} = D_{cent}$. Using the value for $D_{cent}$ determined from the SEM analysis (Fig. 2 and 3), the value for $k$ = 2.28 nm V$^{-1}$ is estimated for PAA-assisted zirconium anodization in 1.5 M $H_2SeO_4$. The obtained $k$-value can be used to calculate the value for $D_{cent}$ as a function of $U_a$, given that the same electrolytic conditions are utilized. Interestingly, the $k$-value obtained in this work differs from $k$ = 2.50 nm V$^{-1}$ commonly accepted for PAA formed in the usual electrolytes[36] but closely matches the values previously reported for aluminum anodization in selenic acid solutions of the same and similar concentrations.[24,37]

Once the $k$-value is obtained, the population density for both the pores and $ZrO_2$ nanostructures can be estimated, assuming that each pore reaching the Zr underlayer generates zirconium oxide underneath and inside the pore:

$$\rho_N = 1.15/(k \cdot U_a)^2 \quad (2)$$

Furthermore, the $U_a$-value determines the pore diameter ($d_p$):[36]

$$d_p = k_p \cdot U_a \quad (3)$$

where $k_p$ is known to be exceptionally low in the selenic acid electrolytes (~0.38 nm V$^{-1}$) compared, for example, with $k_p$ = 0.6 nm V$^{-1}$ for anodization in oxalic acid.[24,37] Such a small $k_p$-value revealed for the present case is explained by the narrowest pores (or the lowest porosity ($P = 0.907 \cdot d_p^2/D_{int}^2$) of about 2–3%),[36] which results in the thinnest oxide nanorods synthesized in the selenic acid.[24]

Finally, the length of the rods ($h$) is directly related to the re-anodizing voltage ($U_r$), as may be expected based on the previously reported results for PAA-assisted re-anodization of Zr or Ta in oxalic-acid electrolytes:[17,38]

$$h = k_h \cdot U_r \quad (4)$$

where the value for $k_h$ = 1.0 nm V$^{-1}$ was obtained in the present study.

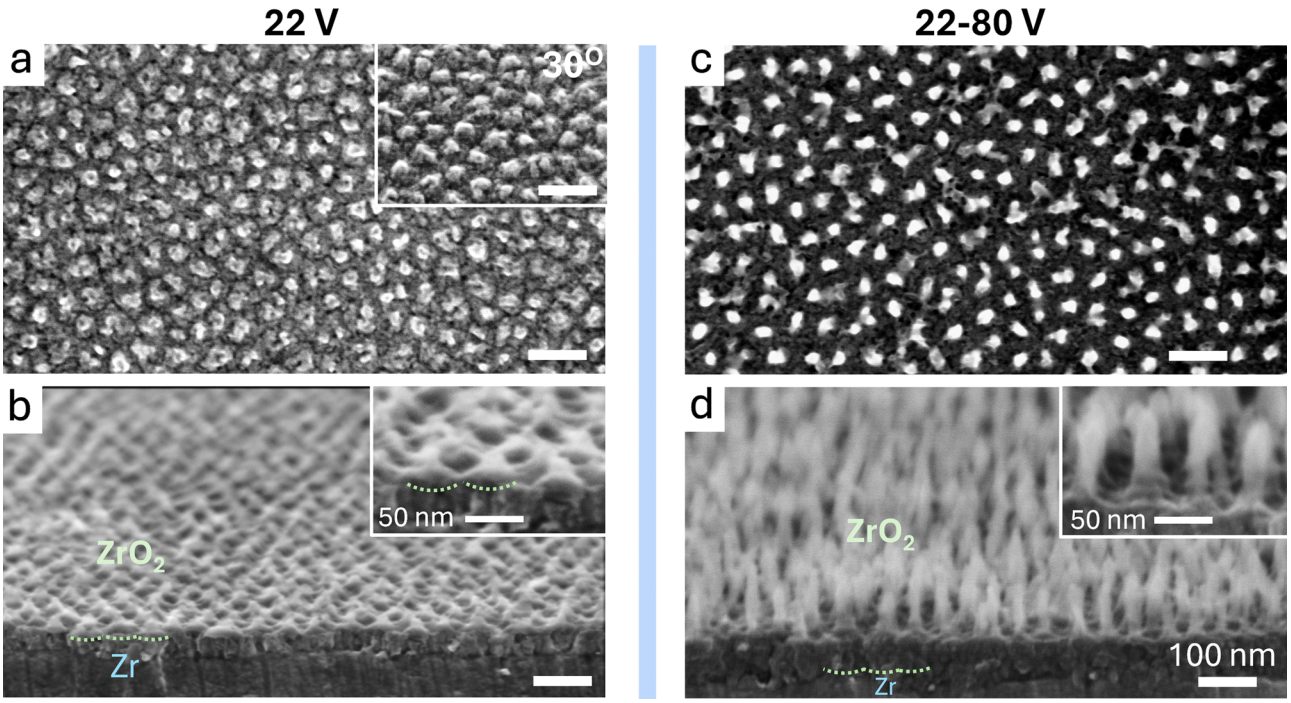


Fig. 2 SEM (a) and (c) surface and (b) and (d) cross-sectional views of $ZrO_2$ nanostructures synthesized *via* (a) and (b) anodization at $U_a$ = 22 V (sample 22 V) followed by (c) and (d) re-anodization to 80 V (sample 22–80 V) of the Al/Zr bilayer in 1.5 M selenic acid as shown in Fig. 1a. The PAA layer was selectively dissolved before SEM observation. The dotted lines over the cross-sectional images point out the $ZrO_2$/Zr interfaces. All undefined scale bars are 100 nm.

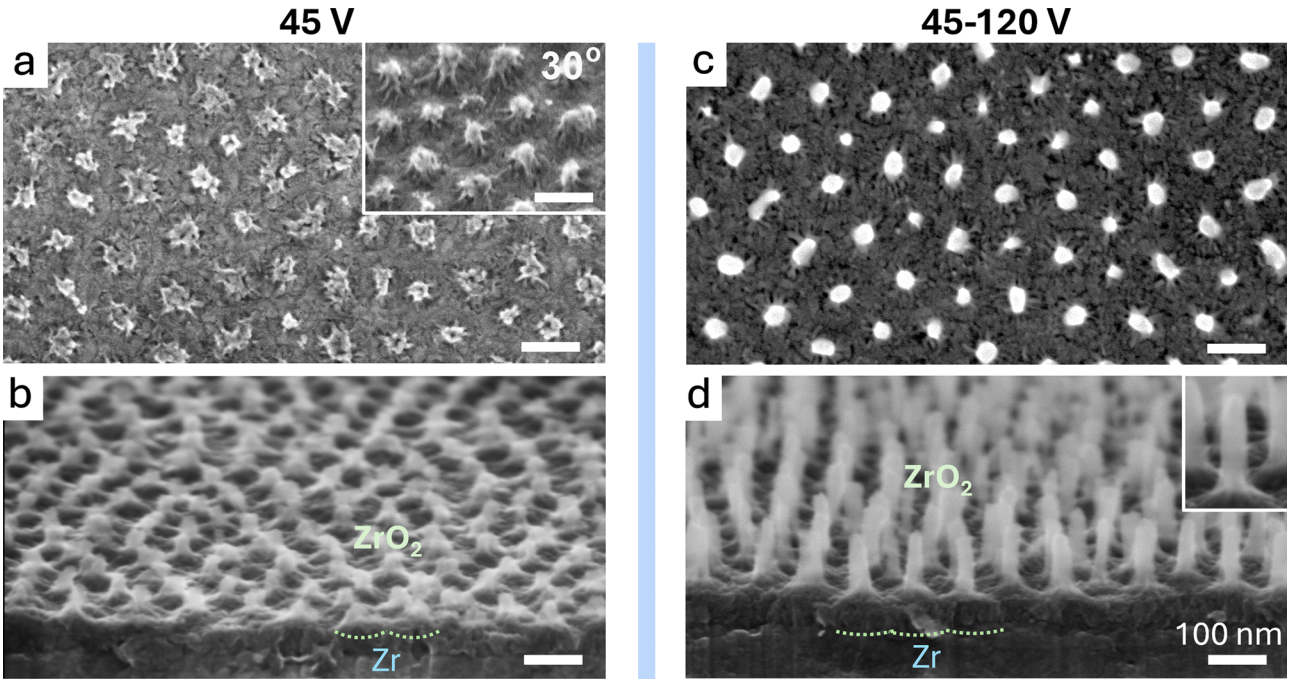


Fig. 3 SEM (a) and (c) surface and (b) and (d) cross-sectional views of $ZrO_2$ nanostructures synthesized *via* (a) and (b) anodization at $U_a$ = 45 V (sample 45 V) followed by (c) and (d) re-anodization to 120 V (sample 45–120 V) of the Al/Zr bilayer in 1.5 M selenic acid as shown in Fig. 1b. The PAA layer was selectively dissolved before SEM observation. The dotted lines over the cross-sectional images point out the $ZrO_2$/Zr interfaces. All undefined scale bars are 100 nm.

Conclusively, based on the anodizing and re-anodizing voltages, the geometrical parameters of the PAA-assisted $ZrO_2$ nanostructures can be pre-determined and adjusted on demand in a certain range.

 

Table 1 Relationship between the formation conditions and geometrical parameters of zirconium-oxide nanostructure arrays formed *via* the PAA-assisted anodization/re-anodization of Zr in 1.5 M selenic acid

| Sample code | Sample nick name | Anodizing voltage ($U_a$), V | Re-anodizing voltage ($U_r$), V | Schematics | Center-to-center distance ($D_{cent}$), nm | Equivalent diameter ($d_n$), nm | Length ($h$), nm | Population density ($\rho_N$), $10^{10}$ cm$^{-2}$ | Bottom-oxide thickness, nm |
|---|---|---|---|---|---|---|---|---|---|
| 22 V | Small nanocones | 22 | — | | 50 | — | 20 | 4.6 | 10 |
| 22–80 V | Small nanorods | 22 | 80 | | 50 | 20 | 90 | 4.6 | 50 |
| 45 V | Big nanocones | 45 | — | | 103 | — | 55 | 1.1 | 10–20 |
| 45–120 V | Big nanorods | 45 | 120 | | 103 | 30 | 120 | 1.1 | 50 |

**Oxide composition.** It is challenging to investigate the composition of valve-metal anodic oxides using optical methods such as Raman spectroscopy because fluorescent organic, phosphoric, or fluoride anions are incorporated into the oxide,[39] causing noisy halos in the Raman spectra due to the intrinsic overlap of the Raman scattering with fluorescence[24,40] and hindering characteristic bands.[41] The incorporation of selenic species in anodic oxides is an exception, as they have been proven not to generate any fluorescent response,[24,41] thus making Raman spectroscopy highly appropriate for the present study. The Raman spectra of the four nanostructured samples shown in Fig. 4 feature well-resolved characteristic bands associated with monoclinic (m) $ZrO_2$[42,43] (marked with a hash sign). The m-$ZrO_2$-related signal obtained from the re-anodized 22–80 V and 45–120 V samples is substantially stronger compared with the anodized 22 V and 45 V samples, meaning that the absolute amount of m-$ZrO_2$ is more significant in the re-anodized films. With reference to the previous works,[17,44] the anodic oxide filling the PAA pores is amorphous, whereas the bottom oxide is polycrystalline. Therefore, the characteristic m-$ZrO_2$ bands are thought to arise from the bottom-oxide layer, separating the oxide developed in the pores from the remaining Zr metal. The intensity of m-$ZrO_2$ peaks in the Raman spectra increasing with the thickening of the bottom oxide reinforces the suggestion that the m-$ZrO_2$ phase resides in the bottom-oxide layer.

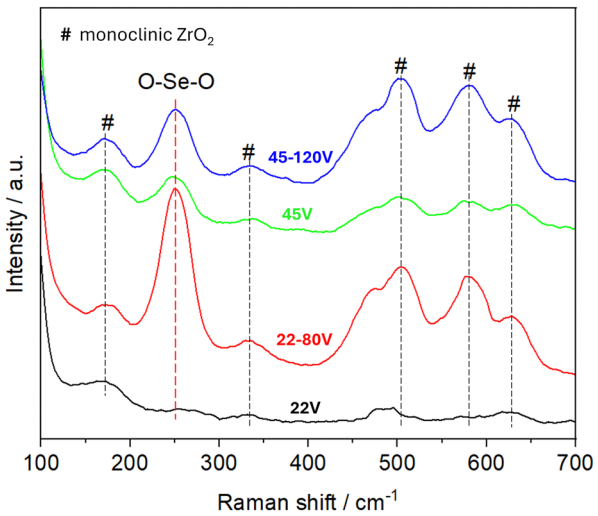


Fig. 4 Raman spectra of the Se-doped small $ZrO_2$ nanocones (sample 22 V), Se-doped small $ZrO_2$ nanorods (sample 22–80 V), Se-doped big $ZrO_2$ nanocones (sample 45 V), and Se-doped big $ZrO_2$ nanorods (sample 45–120 V), as shown in Fig. 1–3. The PAA layers were selectively dissolved before spectra acquisition.

The Raman spectra also feature a characteristic band at 253 cm$^{-1}$ due to O–Se–O vibrations,[45] assuming the incorporation of selenate anions into the oxide structure during the film growth. Comparing the intensities of the 253 cm$^{-1}$ peaks for the anodized and reanodized samples of the same type, one may conclude that the amount of selenium-containing species increases with re-anodization.

The chemical composition and bonding states at the surface layer of the nanostructured and flat anodic films were examined by XPS. The compact anodic films formed in the selenic and phosphoric acids will be hereafter referred to as the 'Se-doped' and 'Se-free' flat $ZrO_2$, respectively.

The recorded narrow spectra of the 45 V and 45–120 V samples appeared very similar to those of the 22 V and 22–80 V samples, respectively. Therefore, in Fig. 5, we only present the detailed analysis of the XP surface spectra of the 22 V (small nanocones) and 22–80 V (small nanorods).

The following elements of interest are identified in the survey spectra of the nanostructured films: C, O, Zr, Al, and Se. Both flat anodic films contain C, O, and Zr, while Se-doped flat film features a significant presence of Se. Narrow-scan C 1s, O 1s, Zr 3d, Al 2p, and Se 3d spectra were acquired to analyze the core levels and bonding states of the elements. The experimental and fitted Zr 3d and Se 3d spectra are shown in Fig. 5. The corresponding C 1s, O 1s, and Al 2p spectra are presented in the ESI† (Fig. S3). In addition, the XP spectra for the 45 V (big nanocones) and 45–120 V (big nanorods) samples are displayed in Fig. S2 (ESI†). A detailed analysis of some of the spectra is available in the ESI,† including the deconvolution of Se Auger peaks overlapping with Zr 3d doublets, the deconvolution of Se 3d spectra, and the deconvolution of O 1s spectra considering the adventitious carbon contribution, to precise the O:(Zr + Al) ratios.

The analysis of Zr 3d spectra (Fig. 5 left column and Fig. S2a and b, ESI†) is complicated by the two broad Se Auger peaks overlapping with Zr 3d doublets. These Se peaks are best seen in the spectrum of the Se-doped flat surface (Fig. 5e). One of them appears as an 'increased background' at binding energies (BE)

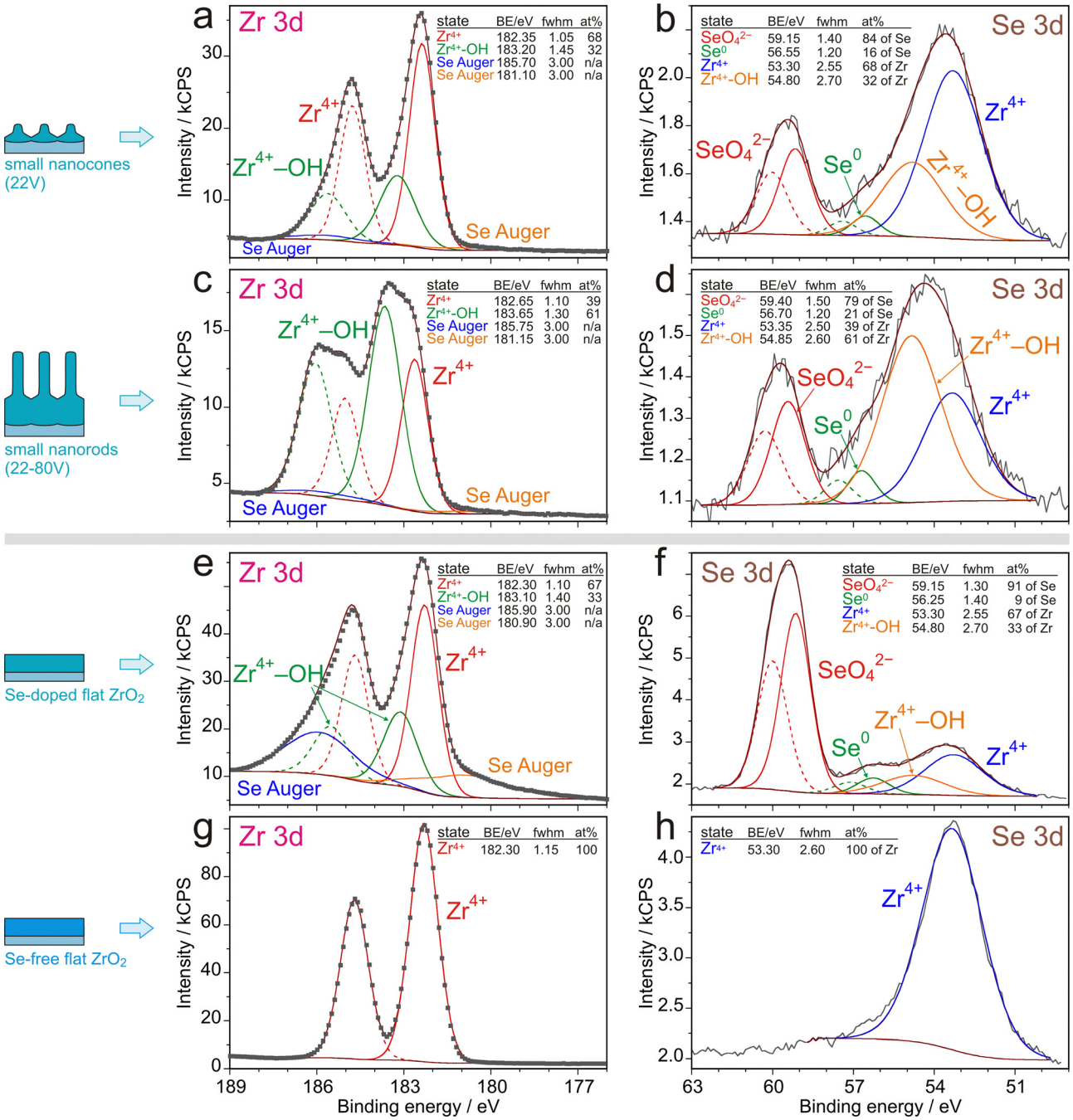


Fig. 5 Experimental and curve-fitted narrow-scan (left column) Zr 3d and (right column) Se 3d XP spectra of the (a) and (b) Se-doped small $ZrO_2$ nanocones (sample 22 V), (c) and (d) Se-doped small $ZrO_2$ nanorods (sample 22–80 V), (e) and (f) Se-doped flat $ZrO_2$ (anodized in 1.5 M $H_2SeO_4$ to 20 V), and (g) and (h) Se-free flat $ZrO_2$ (anodized in 0.1 M $H_3PO_4$ to 20 V).

below the Zr 3d components, while another one 'broadens' the high-BE Zr 3d peaks. The Se peaks are less evident in the Zr 3d spectra of the nanostructured samples (Fig. 5a, c and Fig. S2a, b, ESI†). The initial information about the positions, mutual intensities, and Se 3p-related intensity of the two Se Auger peaks is inherited from the wide spectra of Se-doped $NbO_x$ nanocolumns prepared in our previous work.[24] Two Se Auger peaks are added to the Zr 3d region for all Se-containing samples. More details are available in the ESI.†

The Zr 3d transitions are fitted with $3d_{5/2}$–$3d_{3/2}$ doublets, with a constrained spin–orbit splitting of 2.40 eV, a fixed intensity ratio $3d_{5/2}:3d_{3/2}$ of 3 : 2, and a full width at half maximum (FWHM) equal for the $3d_{5/2}$ and $3d_{3/2}$ components.[16,18,46] The spectra of the nanostructured surfaces are all interpreted with two Zr 3d doublets, in addition to the small Se Auger peaks. The lower-BE doublet (Zr $3d_{5/2}$ at 182.5 ± 0.15 eV with a narrower FWHM of 1.05 ± 0.05 eV) is assigned to the $Zr^{4+}$ oxidation state in $ZrO_2$,[16,18,46] whereas the higher-BE

doublet (Zr $3d_{5/2}$ at 183.5 ± 0.25 eV with a broader FWHM of 1.4 ± 0.05 eV), shifted to +1.0 ± 0.1 eV from the $Zr^{4+}$ doublet, is attributed to hydroxylated $ZrO_2$, *i.e.* $Zr^{4+}$ cations coordinated also with $OH^-$ group(s).[16] The relative amount of the $Zr^{4+}$–OH component increases after the re-anodization from 32 to 61% in the small nanorods and from 43 to 62% in the big nanorods. Thus, the surface of the re-anodized coatings contains more $Zr^{4+}$–OH than $Zr^{4+}$ in $ZrO_2$. The XP spectrum of the Se-doped flat film (Fig. 5e) also shows an intense $Zr^{4+}$–OH doublet (33%) in addition to $ZrO_2$ peaks and pronounced Se Auger peaks. In contrast, the surface of the Se-free flat $ZrO_2$ anodic film (Fig. 5g) contains pure $ZrO_2$.

The presence of $Zr^{4+}$–OH coordination is further confirmed by a detailed analysis of the O 1s spectra (Fig. S2g, h and S3, ESI†), aiming at finding a reliable –OH contribution[47] and relating its intensity with the intensities of the $Zr^{4+}$–OH doublets in the Zr 3d spectra. The details of the procedure for the deconvolution and the results are presented in the ESI.†

The hydroxylated $ZrO_2$ found in large quantities in the surface layer of the oxide nanostructures synthesized in the selenic-acid electrolyte contrasts previous reports on PAA-assisted anodization of zirconium in oxalic or phosphoric acids.[16,18,20] Another difference is the absence of zirconium suboxides in the selenic-acid synthesized nanostructures.[16,18,20] Similarly to previous works,[16,18,20] no residues of metallic zirconium ($Zr^0$) are XPS-detected in the zirconium-oxide nanostructures formed in the selenic acid, which means a complete coverage of the remaining zirconium metal by the anodic oxide. Therefore, the outmost material of all the nanostructures prepared *via* the PAA-assisted anodization in the selenic acid is a mixture of stoichiometric $ZrO_2$ with a large amount of hydroxylated $ZrO_2$, which can be expressed as $ZrO_{2-x}(OH)_{2x}$.

The Al 2p spectra of the anodic-oxide nanostructures (Fig. S2e, f and S3a, d, ESI†) are fitted with a single symmetrical peak associated with $Al_2O_3$ (74.75 ± 0.05 eV with a FWHM of 1.8 ± 0.1 eV). No $Al^0$ is detected on the sample surfaces, meaning that the Al layer was fully converted to PAA after completing Stages I and II (Fig. 1). As expected, no traces of aluminum ($Al^{3+}$ or $Al^0$) are XPS-detected on the surfaces of the flat samples.

An estimation of Zr and Al contents in the nanostructured oxides is performed using the Al 2p and Zr 3d narrow scans after subtracting the areas belonging to the Se Auger peaks in the Zr 3d spectra. Provided that at% (Zr + Al) = 100%, the surface layers contain 65–75 at% Al. This means that the outmost material of the anodic-oxide nanostructures is composed of hydroxylated $ZrO_2$ mixed with $Al_2O_3$. The inner material composing the nanorods, which forms inside the PAA nanopores, is alumina-free. This finding agrees with previous reports on the PAA-assisted N-doped $TiO_2$[48] and Se-doped $Nb_2O_5$ nanostructures[24] containing 50–80 at% $Al^{3+}$ ($Al_2O_3$).

The analysis of the Se 3d spectra (Fig. 5 right column, Fig. S2c and d, ESI†) is the most complex due to its overlapping with Zr 4s. The Se 3d transitions are fitted with $3d_{5/2}$–$3d_{3/2}$ doublets having a constrained spin–orbit splitting of 0.86 eV, a fixed intensity ratio $3d_{5/2}$ : $3d_{3/2}$ of 1.39, and a FWHM equal for the $3d_{5/2}$ and $3d_{3/2}$ components.[24,49] Further Se 3d spectra analysis details are available in the ESI.† In an energy window of ~51–56 eV, the spectra of the nanostructured coatings are fitted with two Zr 4s peaks originating from the $ZrO_2$ oxide and $Zr^{4+}$–OH coordination (in agreement with the Zr 3d spectra; more details are available in the ESI†), whereas at higher BEs, there are two Se 3d doublets associated with selenate (Se $3d_{5/2}$ at 59.3 ± 0.15 eV; ~80%) and elemental selenium (Se $3d_{5/2}$ at 56.65 ± 0.1 eV; ~20%). The spectrum of the Se-doped flat surface (Fig. 5f) also contains selenate (~90%) and $Se^0$ (~10%) doublets, whereas the spectrum of the Se-free flat surface (Fig. 5h) does not have any selenium peaks, as expected, and consists of a single Zr 4s peak due to $ZrO_2$. The fitted BE for Se $3d_{5/2}$ transition in selenate is supported by the modern literature reports,[50,51] including our previous investigation of the Se-doped $NbO_x$ nanocolumns grown in the selenic acid (Se $3d_{5/2}$ at 58.8 ± 0.4).[24] We believe that associating the lower-intensity Se 3d doublet with elemental selenium (for more details, see the ESI†), despite being positioned at a slightly higher BE than reported in the literature (Se $3d_{5/2}$ at 55.4 ± 0.7 eV),[50] is supported by the narrower FWHM than the selenate doublets have and by shifting the peak away from the BE reported for selenide and revealed in the Se-doped $NbO_x$ nanocolumns (Se $3d_{5/2}$ at 54.0 ± 0.5 eV).[24] The presence of $Se^0$ is also assumed from the interpretation of the Raman spectra since the characteristic O–Se–O vibrations identified at 253 $cm^{-1}$ (Fig. 4) overlap with Se–Se vibrations.

The area of Se 3d doublets (excluding the contribution of Zr 4s peaks) is used to calculate the amount of Se at the film surface (provided that at% (Zr + Al + Se) = 100%), after subtracting the contribution of the Se Auger peaks from the Zr 3d spectra. The nanostructured coatings have 1.1–1.6 at% Se, whereas the Se-doped flat surface shows 24 at% Se (76 at% Zr, no Al). The selenate anions are expected to replace a portion of $O^{2-}$ (and possibly $OH^-$) anions in the oxides. In contrast, the elemental selenium may be present as Se nanoparticles encapsulated in the oxide structure or adsorbed on the film surface.

Summarizing the XPS results, the outer layer of the anodic-oxide nanostructures comprises hydroxylated $ZrO_2$, $Al_2O_3$, and $SeO_4^{2-}$ ions replacing a portion of $O^{2-}$ (and possibly $OH^-$) anions, as outlined in Table 2. An overall chemical formula can be derived to address the composition of the surface layer of the anodic films formed *via* the PAA-assisted anodization in the selenic acid, $aZrO_{2-x}(OH)_{2x}{\cdot}bAlO_{1.5}$, with a portion of $O^{2-}$ anions replaced by selenate anions:

$$Zr_aAl_bO_{a(2-x)+1.5b-y}(OH)_{2ax}(SeO_4)_y \quad (5)$$

where parameters $a$, $b$, $x$, and $y$ are available from the XPS analysis (see the ESI,† and Table S2). This formula is verified by calculating O:(Zr + Al) ratios in two different ways: from the chemical formula and using the deconvoluted O 1s spectra (see the ESI†).

**Model of anodic oxide growth.** Based on the experimental findings and with reference to previous works,[16–18] we propose a model for the nucleation and growth of PAA-assisted

Table 2 XPS-determined surface chemistry of the zirconium-oxide nanostructures formed *via* the PAA-assisted anodization/re-anodization in 1.5 M selenic acid and the flat anodic films formed by anodizing zirconium in 1.5 M selenic acid and 0.1 M phosphoric acid[a]

| | | Hydroxylated zirconium dioxide, $ZrO_{2-x}(OH)_{2x}$ | | | Related to Se | | | | O:(Zr + Al) | |
|---|---|---|---|---|---|---|---|---|---|---|
| Sample code | Sample nick name | Zr 3d: $Zr^{4+}$ : $Zr^{4+}$–OH | $x$ | Zr : Al ratio (= 100a : 100b) | at% of Se (Se + Zr + Al = 100 at%) | % of $O^{2-}$ replaced by selenate | $SeO_4^{2-}$ : $Se^0$ | $y$ | Formula-based | O 1s-based |
| 22 V | Small nanocones | 68 : 32 | 0.16 | 35 : 65 | 1.6 | 0.77 | 83 : 17 | 0.013 | 1.77 | 1.61 |
| 22–80 V | Small nanorods | 39 : 61 | 0.305 | 26 : 74 | 1.4 | 0.65 | 79 : 21 | 0.011 | 1.74 | 1.79 |
| 45 V | Big nanocones | 57 : 43 | 0.215 | 34 : 66 | 1.1 | 0.50 | 79 : 21 | 0.009 | 1.77 | 1.68 |
| 45–120 V | Big nanorods | 38 : 62 | 0.31 | 32 : 68 | 1.5 | 0.66 | 78 : 22 | 0.012 | 1.80 | 1.79 |
| Flat 20 V film ($H_2SeO_4$) | Se-doped flat $ZrO_2$ | 67 : 33 | 0.165 | 100 : 0 | 24 | 13 | 91 : 9 | 0.284 | 3.02 | 2.78 |
| Flat 20 V film ($H_3PO_4$) | Se-free flat $ZrO_2$ | 100 : 0 | 0 | 100 : 0 | 0 | 0 | n/a | 0 | 2.00 | 1.99 |

[a] The chemical composition of the outer layer of the anodic films is expressed as a mixture of hydroxylated $ZrO_2$ and $Al_2O_3$ (*i.e.* $a ZrO_{2-x}(OH)_{2x} \cdot b AlO_{1.5}$), having a portion of $O^{2-}$ (and maybe $OH^-$) anions replaced by selenate anions, which can be written as $Zr_aAl_bO_{a(2-x)+1.5b-y}(OH)_{2ax}(SeO_4)_y$, where $a$, $b$, $x$, $y$ are parameters available from the XPS analysis.

zirconium-oxide nanostructures in the selenic-acid electrolyte associated with the small and big nanocones and nanorods synthesized in the present study.

At Stage I (Fig. 1), the Al layer is transformed into PAA layer (Fig. 6a and e). At the commencement of Stage II, zirconium-oxide nanoprotrusions penetrate the PAA barrier layer (Fig. 6b and f) and slightly come out in the pores. Simultaneously, a relatively thin layer of $ZrO_2$ bottom oxide is formed radially, resulting in a wavy $ZrO_2$/Zr interface (Fig. 6b and f). With re-anodization, the protrusions grow further, filling the pores and acquiring the shape of rods, partially mixing with the outmost layer of alumina cell walls (Fig. 6c and g). The bottom-oxide layer thickens accordingly with re-anodizing voltages.

Thus, unlike the barrier-type anodization of Zr when crystalline $ZrO_2$ grows predominantly at the oxide/metal interface with the transport number for cations ($t_{Zr}$) being almost zero,[52,53] the PAA-assisted anodization of Zr is an exceptional case as the zirconium oxide grows partially amorphous and at both the oxide/metal and electrolyte/oxide interfaces. As anodic zirconium oxide develops inside the pores, the $Al_2O_3/ZrO_2$ interface can be used as a marker plane, as pointed out in Fig. 6, to calculate the value for $t_{Zr}$. The approach has been previously justified for PAA-assisted growth of zirconium and some other metal oxides in the usual electrolytes.[16,17,54]

During the PAA-assisted anodization, the cooperative migration of positively and negatively charged ions ($O^{2-}$, $OH^-$, selenate anions, and $Zr^{4+}$ cations) under the high electric field[17,18,24,36,37,55] results in the formation of $ZrO_2$ nanoprotrusions along with the compact bottom-oxide layer. The nanoprotrusions grow wider than the alumina pores, which was revealed by comparing the pore and nanostructure diameters ($d_p$ and $d_n$, respectively). This is because the cross-migration of ions occurs inside the pores and within the outer layer of the pore walls, resulting in partially mixing $ZrO_2$ with $Al_2O_3$ in the outmost layer of the oxide nanorods.[17] The phenomenon is reflected by high Al : Zr ratios derived from the XPS analysis of the nanostructured anodic films (Fig. 5). As confirmed in previous works,[17,44,54] the innermost material composing the rods is most likely alumina-free $ZrO_2$. Such core/shell structures of the anodic-oxide nanorods prepared in this study are depicted in Fig. 6d and h.

The presence of selenate anions in the rods' shells, originating from the dissociation of selenic acid, was proved by the XPS analysis (Fig. 5). We assume that selenate is also incorporated in the rods' cores and part of the bottom-oxide layer adjacent to the electrolyte–oxide interface, as revealed in the previous work on anodizing Al/Hf metal layers.[44] The Raman spectroscopy analysis also suggested the presence of selenate in the nanostructured anodic films (Fig. 4), featuring a more intense O–Se–O signal in the re-anodized nanorods compared with the anodized nanocones. This reinforces the suggestion that selenate anions are incorporated mainly in the protruding parts of the anodic films. Interestingly, the small nanorods exhibiting the highest-intensity O–Se–O band accumulate the largest amount of selenate in their composition.

Regarding the cation migration, since only $Zr^{4+}$ cations contributed to the Zr 3d spectra, they are the only species

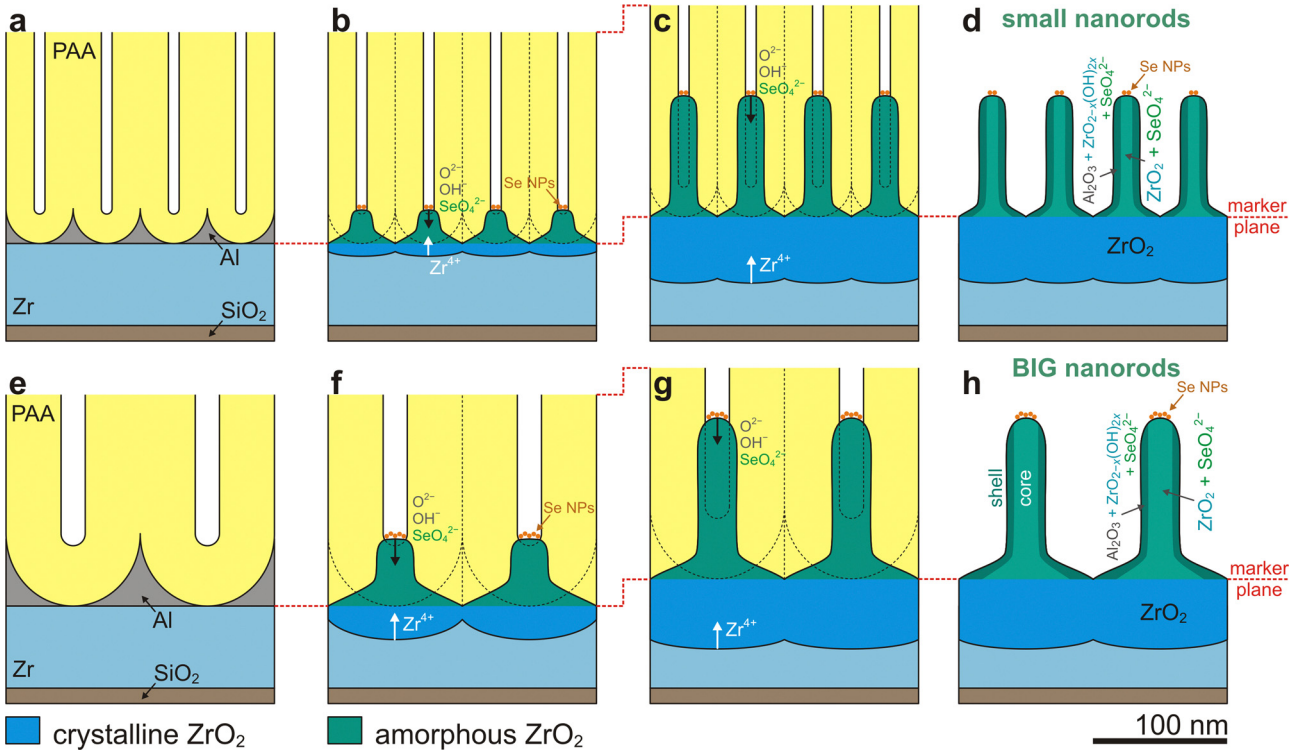


Fig. 6 Schematic model for anodic film growth during the anodization/re-anodization of an Al/Zr bilayer in the 1.5 M selenic-acid electrolyte for forming (upper row) the small nanocone/nanorod samples 22 V and 22–80 V and (lower row) the big nanocone/nanorod samples 45 V and 45–120 V: (a) and (e) the anodization of Al to form the PAA overlayer, (b) and (f) the PAA-assisted Zr anodization to grow zirconium-oxide nanocones under the pores, (c) and (g) the PAA-assisted Zr re-anodization to a higher voltage to grow zirconium-oxide nanorods inside the pores, and (d) and (h) the selective PAA dissolution. The red dashed lines show the position of a marker plane used to calculate the ion transport numbers.

migrating outward under the high field during the anodization/re-anodization. As the amount of hydroxylated $ZrO_2$ increases with re-anodization, the $ZrO_2$–OH coordination is present mainly in the surface layer of the oxide nanorods, not in the bottom oxide.

Based on the above considerations, the formation of nanostructured zirconium oxide accompanied by selenate-ion incorporation may be expressed by the following reactions:

$$Zr^{4+} + (2 - x)O^{2-} + 2xOH^{-} \rightarrow ZrO_{2-x}(OH)_{2x} \quad (6)$$

$$Zr^{4+} + (2 - x - y_a)O^{2-} + 2xOH^{-} + y_a{SeO_4}^{2-} \rightarrow ZrO_{2-x-y,a}(OH)_{2x}(SeO_4)_{y,a} \quad (7)$$

where $x$ and $y_a$ denote the portions of $O^{2-}$ anions replaced by $OH^{-}$ and ${SeO_4}^{2-}$ groups, respectively.

The crystallinity of the films, confirmed by Raman spectroscopy, is associated with the formation of monoclinic $ZrO_2$ in the bottom oxide layer, whereas the nanorods grow in an amorphous manner,[16] consisting of hydroxylated $ZrO_2$, partially mixed with alumina in the outmost layer and doped with selenate anions. Furthermore, it looks paradoxical that the thickness of the bottom-oxide layer is nearly the same (50 nm) in the small- and big-nanorod samples despite the different formation voltages and dissimilar lengths of the rods. However, the value for $t_{Zr} = \sim 0.2$, calculated as described elsewhere,[17,44,54] appeared to be the same for the two systems, although being relatively lower than the value for $t_{Zr} = 0.26$ revealed for the PAA-assisted anodization of zirconium in oxalic acid.[17] This means that, despite the differences in the topography and sizes of the oxide nanorods, the volume of the oxide protrusions that form in the pores is nearly the same for the small and big nanorods.

The last feature worth discussing is the absence of metallic Al and Zr around the oxide nanocones and nanorods, as confirmed by SEM observation and XPS surface analysis after the PAA dissolution in the selective etchant. The phenomenon is explained by the comparable ionic resistivities of $ZrO_2$ nanocones/nanorods and alumina in the PAA barrier layer formed in the selenic acid, which is similar to the Al/Ta anodization[56] and unlike the Al/Ti and Al/Nb anodization.[24,33,48,57] The relatively lower ionic resistance of the underlying $TiO_2$ and $Nb_2O_5$ anodic oxides resulted in concentrating the current mainly in these oxides, leaving the Al, Ti, and Nb metal residues unoxidized around the oxide protrusions.

**Comparison with oxalic acid.** We compared the morphology and chemical composition of the oxide nanorods synthesized in the selenic acid with $ZrO_2$ nanorods grown under similar anodizing and re-anodizing conditions applied to an Al/Zr bilayer in a traditional oxalic-acid electrolyte[17,18] with the following essential findings emerging. The big nanorods prepared in the selenic acid are shorter (120 *vs.* 140 nm) and thinner (30 *vs.* 45 nm in diameter). Moreover, a substantially smaller nanostructure

projected area $A = 0.907 \cdot d_n^2/D_{cent}^2$ (8 *vs.* 17%) was estimated for the big nanorods re-anodized to 120 V in the selenic acid relative to their counterparts formed in the oxalic acid.[17,18] The smaller *A*-value is explained by the low porosity of the PAA layer formed in the selenic acid electrolytes, which makes the PAA-assisted nanostructures exceptionally thin and sharp. In contrast to the present case, $ZrO_2$ nanorods re-anodized to 120 V in the oxalic acid grow with voids in their bottom parts, whereas no void formation occurs in the zirconium-oxide protrusions formed in the selenic acid. The difference may be explained by two-fold shorter re-anodizing current decay in the selenic acid (1 *vs.* 2 min) relative to the oxalic acid.[17] The shorter potentiostatic polarization is expected to result in a relatively minor amount of crystalline m-$ZrO_2$ in the bottom-oxide layer and in suppressing oxygen evolution on the crystallites during the anodizing/re-anodizing processes.[16,57] Furthermore, the big nanorods formed in the selenic acid are anchored to a relatively thinner bottom-oxide layer (50 *vs.* 60 nm). Due to the shorter rods and thinner compact bottom oxide, the overall growth ratio of the PAA-assisted anodic zirconium oxide in the selenic acid is lower (1.42 *vs.* 1.65 nm $V^{-1}$), which is ascribed to the lower relative volume of $ZrO_2$ that forms within the PAA nanopores (~8 *vs.* 17%). This feature makes the films advantageous for potential application to capacitors. Among the similarities between the metal–oxide nanorods formed in the selenic and oxalic acid electrolytes, we notice the absence of Al residues around the oxide nanostructures formed at Stage II. This implies that the difference in the ionic resistivities of $ZrO_2$ nanoprotrusions and the alumina barrier layer is relatively small in the two cases and is hardly affected by the incorporation of selenic-acid- or oxalic-acid-derived species. This feature makes the technology attractive for applications where metallic components are the obstacles.

Concerning the chemical composition of the anodic films, the surface layer of the selenic-acid-made big nanorods contains fully stoichiometric $ZrO_2$, whereas the oxalic-acid-made nanorods comprise a substantial amount of $Zr_2O_3$ suboxide (14%).[18] Furthermore, hydroxylated zirconia ($Zr^{4+}$–OH) is present only in the selenic-acid-made nanorods (62%).[18] In addition, the extent of mixing zirconium oxide with alumina in the outer layer of the big nanorods made in selenic acid seems more significant in comparison with the oxalic-acid-made counterparts, as indicated by the higher Al content (68 *vs.* 25[18] at%, provided that at% (Zr + Al) = 100%).

The above comparison highlights the advantage of the selenic-acid electrolyte for forming the ultra-thin and, therefore, sharp ceramic nanorods composed of stoichiometric $ZrO_2$ mixed with $Al_2O_3$ in the outmost layer, which is also doped with Se species, as it will be discussed in the following section.

**Selenium species in the anodic films.** The $SeO_4^{2-}$ (selenate) anions are incorporated into the oxide structure during the anodization/re-anodization by inward migration of negatively charged $SeO_4^{2-}$ anions under the high electric field with a slower rate relative to $O^{2-}$ and $OH^-$ anions. The following three main differences are noted in incorporating Se species during the PAA-assisted zirconium anodization and recently reported PAA-assisted niobium anodization[24] in selenic acid electrolytes of the same concentration and practically at the same formation voltages: (1) the concentration of Se species revealed in the surface layer of the $ZrO_2$ nanorods is about 3-fold lower than that of the $NbO_x$ nanocolumns (1.4 *vs.* 4.3 at% Se, given that Se + Zr/Nb + Al = 100 at%). (2) Substantial amounts of selenide ($Se^{2-}$) anions along with selenate anions (~50 : 50) are found in the surface layer of the $NbO_x$ nanocolumns, whereas $ZrO_2$ nanorods contain only selenate ($SeO_4^{2-}$) and a minor amount of elemental selenium ($Se^0$). (3) The Se-doped flat $ZrO_2$ surface has far more Se species than the Se-doped flat $Nb_2O_5$ surface[24] (24 *vs.* 10 at% Se, given that Se + Zr/Nb = 100 at%).

The amount of selenate anions in the $ZrO_2$ nanostructures is ~1.7 times lower than that in the $NbO_x$ nanocolumns. Such a difference can be explained by a shorter current decay during the potentiostatic anodization and re-anodization (Stages II and III) of the Al/Zr bilayer (2.5 min) relative to the Al/Nb bilayer (5–10 min). Moreover, the relatively minor $Se^0$ surface contamination of the $ZrO_2$ nanorods does not compete with a more substantial amount of selenide anions revealed on the surface of the $NbO_x$ nanocolumns.[24]

The presence of selenide in the niobium anodic oxide is explained by the reduction of selenate anions on the cathode, followed by the diffusion of the formed $HSe^-$ to the anode and incorporation of $Se^{2-}$ (upon losing a proton) into the oxide structure under the high electric field, in parallel with the migration of $O^{2-}$ and selenate anions. The diffusion of selenide ions is the limiting step; a specific time is required for the selenide ions to reach the electrolyte/oxide interface in an amount sufficient for performing the 'mission'. The flat Se-doped $NbO_x$ film, which was anodized only ~2 min, does not contain any selenide anions, whereas the PAA-assisted $NbO_x$ nanostructures do as they were anodically polarized as long as 15 min.[24] It is assumed that the short anodizing/re-anodizing time employed in the present study is insufficient to achieve an appreciable concentration of $Se^{2-}$ anions near the anode surface to expect the migration of $Se^{2-}$ anions into the growing anodic zirconium oxide.

Still, elemental Se is formed and gradually deposited on the cathode by the reduction of selenate anions *via* the two step reactions:[24,58–60]

$$SeO_4^{2-} + 3H^+ + 2e^- \rightarrow HSeO_3^- + H_2O \quad (8)$$

$$HSeO_3^- + 5H^+ + 4e^- \rightarrow Se^0 + 3H_2O \quad (9)$$

The deposit partially disperses in the electrolyte and is re-deposited as Se nanoparticles on the tops of the rods inside the PAA nanopores or on the surface of Se-doped flat anodic film. After the PAA dissolution, the Se nanoparticles remain on the rods' tops, as shown schematically in Fig. 6. This explanation is reinforced by comparing the total area of the Se $3d_{5/2}$ peak of elemental selenium in the XP spectra of the various anodic films (Fig. 5 and Fig. S2, ESI†): it is the same for the four PAA-assisted nanostructured surfaces (100 ± 10 CPS eV), whereas it is 6-fold larger for Se-doped flat anodic films (580 CPS eV) having apparently wider surfaces available for the nanoparticle deposition.

 

The 2-fold higher amount of surface selenate detected in Se-doped flat $ZrO_2$ films compared with the Se-doped flat $NbO_x$ films[24] may be due to the higher voltage applied for forming the zirconium-oxide films (20 V) relative to the niobium-oxide films (10 V).

A significant revelation from the above consideration is that the amount and chemical composition of Se-containing species incorporated in and adsorbed on the $ZrO_2$ nanorods from the electrolyte may be governed by controlling the current decay at Stages II and III.

### Part II: Antibacterial properties

**Bacteria/surface interfaces.** The interaction of *E. coli* and *S. aureus* with various surfaces prepared in this work was studied by analyzing the SEM images after culturing bacteria on the nanostructured and flat anodic films. Following a 5-hour incubation, the samples were gently washed with PBS to remove unattached bacteria. The attached bacteria were then processed through dehydration steps for SEM imaging. The representative top and 3D SEM views of the bacteria fixed on each surface are displayed in Fig. 7. The extended collection of 3D SEM images related to this study is available in the ESI.†

The top views show that *E. coli* keep their typical elongated shapes (Fig. 7a, b, e, and f). However, the bacteria have significant length variability depending on substrate type, and a visible shape distortion is observed for bacteria residing on the nanostructured surfaces. An unusual membrane projection

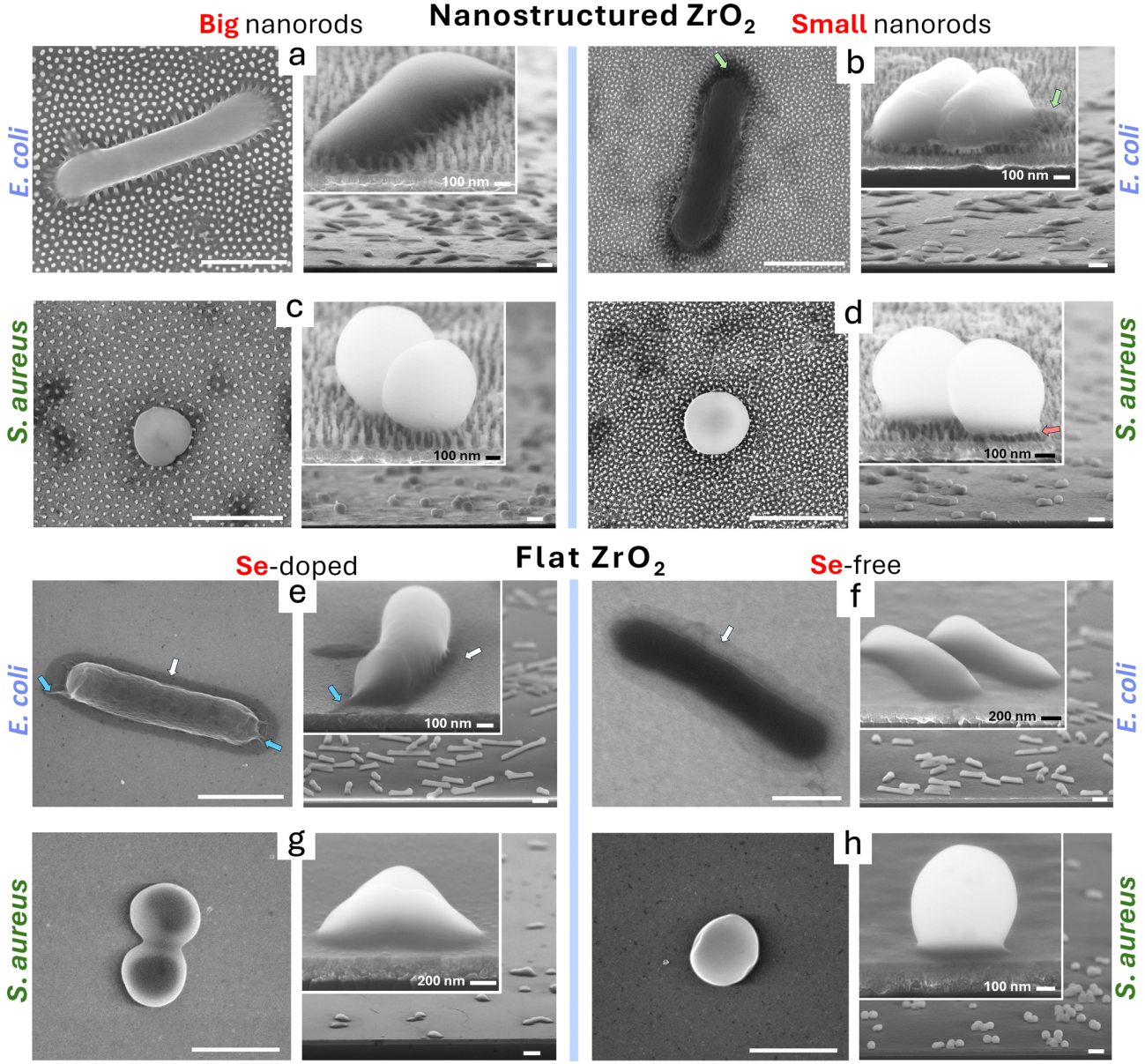


Fig. 7 Typical SEM surface and 3D views of *E. coli* and *S. aureus* bacteria residing on the (a) and (c) Se-doped big $ZrO_2$ nanorods, (b) and (d) Se-doped small $ZrO_2$ nanorods, (e) and (g) Se-doped flat $ZrO_2$, and (f) and (h) Se-free flat $ZrO_2$. The nanostructured surfaces were prepared and are coded as shown in Fig. 1–3 and Table 1. All undefined scale bars are 1 μm.

around the cells is noted on the small nanorods and Se-doped flat and Se-free flat surfaces (Fig. 7b green arrows and Fig. 7e and f white arrows). Besides, a few protrusions are visible for bacteria residing on the Se-doped flat surface (Fig. 7e, blue arrows). The 3D SEM images deepen the insight into the film-bacteria interaction. *E. coli* cells are visibly stretched out when contacting the big nanorods, with individual nanorods fully piercing the bacteria membranes. A different behavior of *E. coli* is observed on the small nanorods. *E. coli* reside on the rods' tops without complete cell membrane penetration by the rods. However, the thin membrane-like substance spread around and pinned on the rods may result from intracellular tension (Fig. 7b, green arrows) damaging/rupturing the bacterial membrane at the bacteria/rod interface. The *E. coli* residing on the flat surfaces also undergo significant stress, leading to shape distortion, membrane tension, and substantially extending the cell/film interface.

From the SEM images of *S. aureus*, the bacteria spread character and, therefore, the shapes and diameters of their cells depend on the substrate type. An irregular shape on the big nanorods, membrane craters, and a partial engulfment of the nanorods into the bacteria membranes is noted (Fig. 7c). No stretching of the *S. aureus* membrane is observed here. In contrast, the *S. aureus* membranes undergo significant stretching on the small nanorods, visibly pierced and torn by the rods, which results in apparent membrane damage or rupture (Fig. 7d, red arrow). The unfavorable conditions for *S. aureus* contacting the flat surfaces cause a significant shape distortion, extending the bacterium/substrate contact area and making the bacteria look like a pressed ball (Se-free) or a cone (Se-doped). The SEM observations show that both bacterial strains suffer stress on the flat zirconia surfaces, especially on Se-doped $ZrO_2$.

Fig. 8 shows the modified JIS Z 2801 test assay results after the 24-hour bacteria/substrate incubation. The *E. coli* CFU is systematically reduced in the following order: glass ≥ Se-free flat > Se-doped flat > small nanorods ≥ big nanorods (Fig. 8a), quantitatively confirming the worst experience for the bacteria contacting the nanostructured surfaces observed by SEM. The data show no significant differences between the glass and Se-free $ZrO_2$ surfaces, nor between small and big nanorods. However, significant differences were observed between the Se-free and Se-doped flat $ZrO_2$ surfaces and between Se-doped flat surfaces and nanorods, confirming the simultaneous influence of nanostructuring and material composition. A similar trend is noted for the *S. aureus* behavior (Fig. 8b). The *S. aureus* colony count on the nanorods is reduced by approximately 120-fold and 67-fold compared to the control glass and Se-doped flat surfaces, respectively. The reduction in the *E. coli* bacteria count is about 8-fold and 5-fold compared to the glass and Se-doped flat surfaces, respectively. The antibacterial efficacy of the nanorod surfaces, expressed as the percentage of non-viable cells relative to the initial seeding bacterial count, reached approximately 76% for *E. coli* and 99% for *S. aureus.* These results suggest that the Se doping and nanostructuring synergistically enhance the antibacterial efficiency of the films, with greater effectiveness against *S. aureus*.

**Bacteria–surface interaction mechanism.** There has been a continuous interest in engineering antibacterial surfaces and

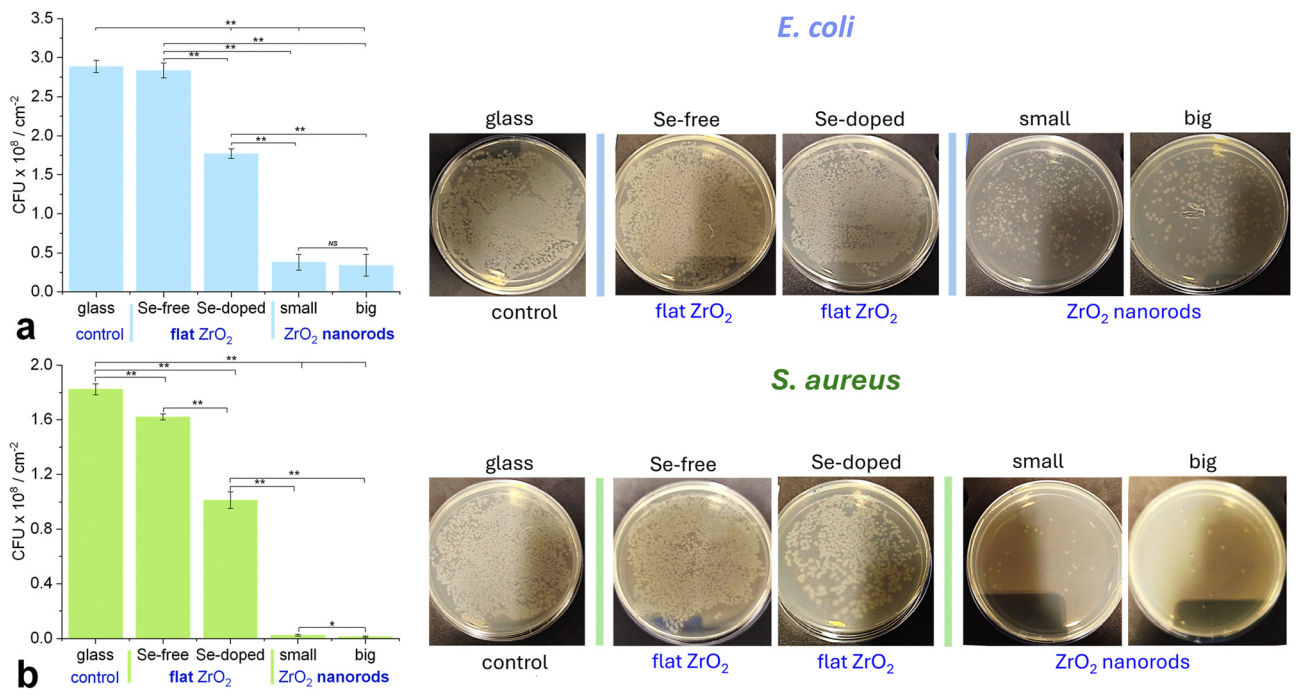


Fig. 8 Colony counting assay evaluating contact killing and antifouling efficacy of $ZrO_2$ nanostructured (small and big nanorods) and flat (Se-free and Se-doped) surfaces in comparison with a glass control against (a) Gram-negative bacteria *E. coli* and (b) Gram-positive bacteria *S. aureus*. The statistical significance is denoted as $^{**}p < 0.001$, $^{*}p < 0.05$, and NS – not significant (Student's *t*-test). Values less than 0.05 were considered statistically significant. Photographs of the assays after the cultivation are shown in the right panels for each bacteria and sample type.

 

implants capable of repelling and/or contact killing a broad spectrum of bacteria since the progress in biomedical science can overcome the worldwide problem of bacterial resistance and poor long-term functional performance of antibacterial coatings based on ion/drug-release mechanisms.[61,62] Therefore, direct preparation of micro- and nanostructured surfaces from polymeric materials, metals, or metal-oxides has a promising future in advancing the fabrication technologies and application perspectives of durable bactericidal materials.[63,64]

To understand the processes occurring at the biointerface between $G^+$ and $G^-$ bacteria and the arrays of Se-doped $ZrO_2$ nanorods, the composition and thickness of $G^+$ and $G^-$ cytoplasmic membranes should be considered. *E. coli* possess complex membrane walls with a typical thickness of ~8 nm. In contrast, $G^+$ cell walls are much thicker, ~30–100 nm.[65] The difference in the cell wall structure and thickness gives the bacteria different levels of protection and stability towards external cues. It is also one of the reasons why the $G^+$ and $G^-$ bacteria interact with the nanostructured surface and chemistry of materials differently. Many reported works have suggested various bacteria damage or killing mechanisms upon interactions with nanostructured materials of various geometry, chemistry, stiffness, or wettability.[66–68] Such mechanisms consider the physical deformation or rupture of the cell wall upon the contact of bacteria with the surface, repellent killing, chemical destabilization of the membrane structure, generation of oxidative stress upon the surface contact, or combinations of the above since various mechanisms may work simultaneously.[69,70]

Based on the SEM examination of the bio-interfaces performed in the present work, we may conclude that *E. coli* spread out on the big nanorods, and the thin cellular walls of their membranes are impaled entirely by the rods in contact with their bodies. The piercing apparently leads to the rupturing of the bacteria membrane and cell death as the rods penetrate the internal *E. coli*'s structure through the thin membrane, ruling out the membrane engulfment of the oxide nanorods. A different state of the bio-interface is noted for the higher-population-density small and thinner nanorods. Due to the interfacial energy gradient, *E. coli* resides on the rods' apexes, bending the rods at the cell edge. Even though the small nanorods do not entirely penetrate the *E. coli* cell, the tension in the bacteria membrane contacting the rods causes membrane damage or rupture. No doubt, the strong attachment of the bacteria to the oxide nanostructures leads to developing cellular stress that is manifested by pushing the cell contents into the center of the cell body and pinning the membrane projection around the cell. Such tension within the bacterial cells can destroy the cell membrane, which is also according to the theoretical prediction.[71] Although numerous studies have reported higher antibacterial efficacy with higher-density nanopillar arrays,[72,73] there have also been contrasting works claiming the opposite effect.[74] Our quantitative *E. coli*-related results do not show any significant differences between the two types of nanorod surfaces. However, the SEM images suggest that the bacteria pierced on the low-density surfaces (big nanorods) and adhered on the higher-density surfaces (small nanorods) were killed by different mechanisms. The observed bacteria cell shape distortion on the flat $ZrO_2$ surfaces can be attributed to inconvenient conditions for the bacteria due to the interaction with anodic zirconium oxide and, especially, Se-doped anodic oxide (Fig. 7e, f and 8a). This comparison shows clearly that the presence of Se species enhances the antibacterial effect of anodic zirconium oxide: doping the surface with Se-containing species inhibits bacterial proliferation, disrupts the usual bacterial lifecycle, and results in visible cellular membrane distortion and reduced bacterial colony count. This is consistent with the literature stating that selenium contributes to eliminating $G^+$ and $G^-$ bacteria.[75–77] However, although the selenium content is higher on the flat surface than on the nanostructured coating, the latter appears markedly more harmful and life-threatening to the bacteria, supposedly owing to the contribution of mechano-penetration generated by the thin and sharp nanorods. Additionally, while the contact killing of adhered bacteria is apparent from the SEM images, the quantitative data show that the surface also prevents the adhesion (antifouling effect), proliferation of *E. coli*, and biofilm formation since the most *E. coli* bacteria remained non-adherent and their counts were significantly reduced from the initial values.

The interaction of *S. aureus* with the nanostructured coatings and the flat surfaces shows several distinct features observed by SEM. Unlike *E. coli*, *S. aureus* resides on the tops of the big nanorods, with only a minor piercing of the bacterial membrane by the rods' tips. Although the bacteria likely lose the ability to move, such penetration into the cytoplasmic membrane of *S. aureus* is insufficient to damage the internal structure because of the high thickness of the cellular wall. Direct penetration into the *S. aureus* membranes due to mechanical puncturing activated by the thinner needle-like small nanorods damages/ruptures the bacteria membranes, resembling the situation with *E. coli* on the small nanorods.

Moreover, the stretching of the cell membranes between the rods beyond a critical value and eventual membrane rupture is likely enhanced by the solid bacterial adhesion to both nanostructures and the bacteria's desperate effort to move away from the uncongenial chemistry and topography.[78]

The comparison of the impacts of the Se-doped nanostructured and flat surfaces on the two types of bacteria shows a synergetic effect enhancing the bactericidal properties: the Se-doped $ZrO_2$ surfaces function as non-metallic (Se) ions releasing bactericidal coatings in addition to the repellent and mechanical puncture activities arising due to the needle-like nanostructuring (contact killing).

To conclude, the nanostructured arrays prepared here appeared more efficient against *S. aureus*, with the antibacterial efficacy reaching 99% (*vs.* 76% against *E. coli*). However, the absence of a standardized testing methodology for evaluating the antimicrobial efficiency of micro- and nanostructured surfaces, often related to material composition and ion release, creates challenges in comparing reported data due to the variations in protocols, incubation time, controls, and result interpretations.[79] For example, antibacterial efficacy should be related to the initial bacterial count independently of the

control sample, and in most cases, it is attributed to a flat surface. The approach requires the bacteria to be placed only on the active nanosurface, ensuring that the surrounding plastic is uninvolved, which often cannot be avoided. Despite some inconsistencies, the antibacterial efficacy of 99% against *S. aureus* has been reported for Au nanostructured surfaces,[80] comparable to our results, but it was 83% for silicon nanostructured films[81] relative to the flat surfaces. The antibacterial efficacy of our samples against *E. coli* appeared to be somewhat lower compared with the best literature reports. For example, nanostructured black silicon has revealed ~97% efficacy,[82] while polycarbonate nanopillars demonstrated similar performance levels.[83] From the sample fabrication viewpoint, the approach developed in the present work is advantageous in allowing the formation of fully self-organized nanostructured surfaces without involving replication techniques, transfer technologies, masks, organic materials, or high-temperature processes. It is anticipated that using an increased concentration of a selenic-acid electrolyte or longer anodizing times to incorporate selenide and selenate ions could further enhance the bactericidal properties of such surfaces. However, adjusting the electrolyte concentration will inevitably influence the growth of the PAA layer, generating different surface morphologies. Further studies are required to systematically address the impact of electrolytic conditions and anodizing variables on the morphology and composition of the PAA-assisted zirconium-oxide nanostructures in pursuit of extending functionalities and applications of these extraordinary nanomaterials beyond the biomedical niche. Potential applications include catalytic and gas-sensing nanomaterials, superhydrophobic and oleophobic surfaces, optical coatings for index-contrast multilayer structures, UV anti-reflective and dielectric mirrors, optical superlattices, and nanocomposites for advanced dielectrics.

## Conclusions

The following conclusions can be drawn from the present study.

1. Two types of arrays of extraordinarily thin systematically self-arranged zirconium-oxide-based nanocones and nanorods upright standing on a substrate were synthesized for the first time *via* the PAA-assisted anodization of Zr in 1.5 M selenic acid. The nanorods formed in the selenic acid are ~1.5-fold thinner than the PAA-assisted $ZrO_2$ nanorods formed in the oxalic acid and ~1.2-fold thinner than the PAA-assisted $Nb_2O_5$ nanorods grown in the selenic acid at the same formation potentials. Thus, the claim of ultra-thin $ZrO_2$-based nanorods is experimentally justified.

2. The nanorods feature a core/shell structure, where the core is stoichiometric $ZrO_2$ and the shell is several-nm-thick amorphous $ZrO_2$ mixed with $ZrO_{2-x}(OH)_{2x}$ and $Al_2O_3$. The cores and shells comprise selenate ($SeO_4^{2-}$) anions, which replace up to 1% of the $O^{2-}$ ions in the surface layer. Besides, nanoparticles of elemental Se are deposited on the top of rods during anodization.

3. The Se-doped nanorods tested as potential antibacterial nanomaterials toward G-negative *E. coli* and G-positive *S. aureus* revealed a destructive synergetic effect on the bacteria, functioning as the non-metallic (Se) ion-releasing bactericidal coatings along with the repellent and contact-killing activities provided by the extraordinary needle-like nanostructures.

4. The technology and properties of the nanostructured arrays developed here may be advantageous for many more potential applications such as gas sensing, catalysis, nano-optics and nano-photonics, electronics, or water- and oil-repelling surfaces. These may be the subjects for future works.

## Author contributions

Kirill Kamnev: conceptualization, methodology, investigation, visualization, formal analysis, and writing – original draft; Maria Bendova: investigation, formal analysis, visualization, validation, and writing – original draft; Zdenka Fohlerova: investigation, formal analysis, visualization, and writing – original draft; Tatiana Fialova: investigation and formal analysis; Oleh Martyniuk: investigation; Jan Prasek: investigation; Kristyna Cihalova: investigation and formal analysis; Alexander Mozalev: methodology, investigation, visualization, writing – review and editing, resources, project administration, and funding acquisition.

## Data availability

The data supporting this article have been included in the ESI.†

## Conflicts of interest

The authors declare that they have no known competing financial interests or personal relationships that could have appeared to influence the work reported in this paper.

## Acknowledgements

The research leading to these results was financially supported by the Czech Science Foundation (GACR), project no. 20-25486S. The CzechNanoLab project LM2023051 funded by the MEYS CR is acknowledged for the financial support of the measurements/sample fabrication at CEITEC Nano Research Infrastructure. K. K. acknowledges the support received from the Jaroslav Koča BRIDGE fund for part of this work.

## References

1 S. Halley, K. Pasupathikovil Ramaiyan, L. Tsui and F. Garzon, A review of zirconia oxygen, NOx, and mixed potential gas sensors – History and current trends, *Sens. Actuators, B*, 2022, **370**, 132363.
2 J. Xie, Z. Zhu, H. Tao, S. Zhou, Z. Liang, Z. Li, R. Yao, Y. Wang, H. Ning and J. Peng, Research progress of high

 

dielectric constant zirconia-based materials for gate dielectric application, *Coatings*, 2020, **10**, 698.
3 S. He, Y. Zou, K. Chen and S. P. Jiang, A critical review of key materials and issues in solid oxide cells, *Interdiscip. Mater.*, 2023, **2**, 111.
4 F. E. Bortot Coelho, G. Magnacca, V. Boffa, V. M. Candelario, M. Luiten-Olieman and W. Zhang, From ultra to nanofiltration: A review on the fabrication of $ZrO_2$ membranes, *Ceram. Int.*, 2023, **49**, 8683.
5 S. Guo, D. Xu, Y. Liang, Y. Gong, Y. Li and J. Yang, Corrosion characterization of $ZrO_2$ and $TiO_2$ ceramic coatings via air plasma spraying on 316 stainless steel in oxygenated sub- and supercritical water, *J. Supercrit. Fluids*, 2020, **157**, 104716.
6 K. Tanabe, Surface and catalytic properties of $ZrO_2$, *Mater. Chem. Phys.*, 1985, **13**, 347.
7 S. J. Malode and N. P. Shetti, $ZrO_2$ in biomedical applications, in *Metal Oxides for Biomedical and Biosensor Applications*, ed. K. Mondal, Elsevier, 1st edn, 2021, ch. 18, p. 471.
8 A. T. Oluwabi, I. O. Acik, A. Katerski, A. Mere and M. Krunks, Structural and electrical characterisation of high-*k* $ZrO_2$ thin films deposited by chemical spray pyrolysis method, *Thin Solid Films*, 2018, **662**, 129.
9 K. Bobzin, E. Lugscheider, M. Maes and P. Immich, Developing PVD zirconium-oxide coatings for use of thixoforming of steel, *Int. J. Microstruct. Mater. Prop.*, 2008, **3**, 262.
10 L. Kumari, W. Z. Li, J. M. Xu, R. M. Leblanc, D. Z. Wang, Y. Li, H. Guo and J. Zhang, Controlled hydrothermal synthesis of zirconium oxide nanostructures and their optical properties, *Cryst. Growth Des.*, 2009, **9**, 3874.
11 J. Mittra, G. J. Abraham, M. Kesaria, S. Bahl, A. Gupta, S. M. Shivaprasad, C. S. Viswanadham, U. D. Kulkarni and G. K. Dey, Role of substrate temperature in the pulsed laser deposition of zirconium oxide thin film, *Mater. Sci. Forum*, 2012, **710**, 757.
12 S. Koyama, Y. Aoki, N. Sakaguchi, S. Nagata and H. Habazaki, Phase transformation and capacitance enhancement of anodic $ZrO_2$–$SiO_2$, *J. Electrochem. Soc.*, 2010, **157**, C444.
13 A. Fattah-alhosseini, R. Chaharmahali, M. K. Keshavarz and K. Babaei, Surface characterization of bioceramic coatings on Zr and its alloys using plasma electrolytic oxidation (PEO): a review, *Surf. Interface*, 2021, **25**, 101283.
14 S. Noothongkaew, K. Ariyachaokun and S. Pansri, Enhanced bioactivity and antibacterial properties of anodized $ZrO_2$ implant coatings via optimized nanoscale morphology and timed antibiotic release through PLGA overcoat, *Ceram. Int.*, 2021, **47**, 33775.
15 G. D. Sulka, Electrochemistry of thin films and nanostructured materials, *Molecules*, 2023, **28**, 4040.
16 A. Mozalev, Z. Pytlicek, K. Kamnev, J. Prasek, F. Gispert-Guirado and E. Llobet, Zirconium oxide nanoarrays via the self-organized anodizing of Al/Zr bilayers on substrates, *Mater. Chem. Front.*, 2021, **5**, 1917.
17 K. Kamnev, M. Sepulveda, M. Bendova, Z. Pytlicek, J. Prasek, E. Kolibalova, J. Michalicka and A. Mozalev, The growth, composition, and functional properties of self-organized nanostructured $ZrO_2$–$Al_2O_3$ anodic films for advanced dielectric applications, *Adv. Electron. Mater.*, 2021, **7**, 2100505.
18 K. Kamnev, Z. Pytlicek, M. Bendova, J. Prasek, F. Gispert-Guirado, E. Llobet and A. Mozalev, The planar anodic $Al_2O_3$-$ZrO_2$ nanocomposite capacitor dielectrics for advanced passive device integration, *Sci. Technol. Adv. Mater.*, 2023, **24**, 2162324.
19 M. Sepulveda, K. Kamnev, Z. Pytlicek, J. Prasek and A. Mozalev, Superhydrophobic–oleophobic visible–transparent antireflective nanostructured anodic $HfO_2$ multifunctional coatings for potential solar panel applications, *ACS Appl. Nano Mater.*, 2021, **4**, 1754.
20 Z. Fohlerova, K. Kamnev, M. Sepulveda, Z. Pytlicek, J. Prasek and A. Mozalev, Nanostructured zirconium-oxide bioceramic coatings derived from the anodized Al/Zr metal layers, *Adv. Mater. Interfaces*, 2021, **8**, 2100256.
21 D. Chopra, A. Jayasree, T. Guo, K. Gulati and S. Ivanovski, Random, aligned and grassy: Bioactivity and biofilm analysis of zirconia nanostructures as dental implant modification, *Composites, Part B*, 2023, **259**, 110725.
22 O. Nishinaga, T. Kikuchi, S. Natsui and R. O. Suzuki, Rapid fabrication of self-ordered porous alumina with 10-/sub-10-nm-scale nanostructures by selenic acid anodizing, *Sci. Rep.*, 2013, **3**, 2748.
23 Y. Nazarkina, K. Kamnev, A. Dronov, A. Dudin, A. Pavlov and S. Gavrilov, Features of porous anodic alumina growth in galvanostatic regime in selenic acid based electrolyte, *Electrochim. Acta*, 2017, **231**, 327.
24 K. Kamnev, M. Bendova, Z. Pytlicek, J. Prasek, L. Kejik, F. Guell, E. Llobet and A. Mozalev, Se-doped $Nb_2O_5$–$Al_2O_3$ composite-ceramic nanoarrays via the anodizing of Al/Nb bilayer in selenic acid, *Ceram. Int.*, 2023, **49**, 34712.
25 R. W. van Nieuwenhoven, A. M. Burger, L. L. E. Mears, P. Kienzl, M. Reithofer, A. Elbe-Burger and I. C. Gebeshuber, Verifying antibacterial properties of nanopillars on cicada wings, *Appl. Nanosci.*, 2024, **14**, 531.
26 J. Holinka, M. Pilz, B. Kubista, E. Presterl and R. Windhager, Effects of selenium coating of orthopaedic implant surfaces on bacterial adherence and osteoblastic cell growth, *Bone Joint J.*, 2013, **95**, 678.
27 O. Bilek, Z. Fohlerova and J. Hubalek, Enhanced antibacterial and anticancer properties of Se-NPs decorated $TiO_2$ nanotube film, *PLoS One*, 2019, **3**, e0214066.
28 X. Chen, J. Zhou, Y. Qian and L. Zhao, Antibacterial coatings on orthopedic implants, *Mater. Today Bio*, 2023, **19**, 100586.
29 X. Chen, K. Cai, J. Fang, M. Lai, Y. Hou, J. Li, Z. Luo, Y. Hu and L. Tang, Fabrication of selenium-deposited and chitosan-coated titania nanotubes with anticancer and antibacterial properties, *Colloids Surf., B*, 2013, **103**, 149.
30 Z. Pytlicek, M. Bendova, J. Prasek and A. Mozalev, On-chip sensor solution for hydrogen gas detection with the anodic niobium-oxide nanorod arrays, *Sens. Actuators, B*, 2019, **284**, 723.
31 A. Mozalev, M. Bendova, F. Gispert-Guirado, E. Llobet and H. Habazaki, Porous-anodic-alumina-templated Ta–Nb-alloy/

oxide coatings via the magnetron-sputtering/anodizing as novel 3D nanostructured electrodes for energy-storage applications, *Surf. Coat. Technol.*, 2024, **489**, 131042.

32 B. P. Payne, M. C. Biesinger and N. S. McIntyre, X-ray photoelectron spectroscopy studies of reactions on chromium metal and chromium oxide surfaces, *J. Electron Spectrosc. Relat. Phenom.*, 2011, **184**, 29.

33 A. Mozalev, R. M. Vázquez, C. Bittencourt, D. Cossement, F. Gispert-Guirado, E. Llobet and H. Habazaki, Formation–structure–properties of niobium-oxide nanocolumn arrays via self-organized anodization of sputter-deposited aluminum-on-niobium layers, *J. Mater. Chem. C*, 2014, **2**, 4847.

34 X-ray photoelectron spectroscopy (XPS) reference pages. Adventitious carbon. **https://www.xpsfitting.com/search/label/Adventitious** (accessed 1-May-2024).

35 V. Surganov, P. Morgen, J. G. Nielsen, G. Gorokh and A. Mozalev, Study of the initial stage of aluminium anodization in malonic acid solution, *Electrochim. Acta*, 1987, **32**, 1125.

36 W. Lee and S.-J. Park, Porous anodic aluminum oxide: anodization and templated synthesis of functional nanostructures, *Chem. Rev.*, 2014, **114**, 7487.

37 T. Kikuchi, O. Nishinaga, S. Natsui and R. O. Suzuki, Self-ordering behavior of anodic porous alumina via selenic acid anodizing, *Electrochim. Acta*, 2014, **137**, 728.

38 A. Mozalev, M. Sakairi and H. Takahashi, Structure, morphology, and dielectric properties of nanocomposite oxide films formed by anodizing of sputter-deposited Ta-Al bilayers, *J. Electrochem. Soc.*, 2004, **151**, F257.

39 S. Ono, Nanostructure analysis of anodic films formed on aluminum–Focusing on the effects of electric field strength and electrolyte anions, *Molecules*, 2021, **26**, 7270.

40 D. Wei, S. Chen and Q. Liu, Review of fluorescence suppression techniques in Raman spectroscopy, *Appl. Spectrosc. Rev.*, 2015, **50**, 387.

41 Y. Nazarkina, K. Kamnev, A. Polokhin and Y. Shaman, The effect of annealing on the Raman spectra of porous anodic alumina films formed in different electrolytes, in 2017 IEEE Conference of Russian Young Researchers in Electrical and Electronic Engineering (EIConRus), 2017, IEEE, DOI: **10.1109/EIConRus.2017.7910834**.

42 G. Stefanic, S. Music, S. Popovic and A. Sekulic, FT-IR and laser Raman spectroscopic investigation of the formation and stability of low temperature t-$ZrO_2$, *J. Mol. Struct.*, 1997, **408–409**, 391.

43 P. Barberis, T. Merle-Mejean and P. Quintard, On Raman spectroscopy of zirconium oxide films, *J. Nucl. Mater.*, 1997, **246**, 232.

44 A. Mozalev, M. Bendova, F. Gispert-Guirado and E. Llobet, Hafnium-oxide 3-D nanofilms via the anodizing of Al/Hf metal layers, *Chem. Mater.*, 2018, **30**, 2694.

45 A. Anderson, A. Sanders and W. Smith, Raman spectra of selenium dioxide at low temperatures, *J. Raman Spectrosc.*, 2000, **31**, 403.

46 X-ray photoelectron spectroscopy (XPS) reference pages, Zirconium. **https://www.xpsfitting.com/search/label/Zirconium** (accessed 1-May-2024).

47 J. Cerezo, P. Taheri, I. Vandendael, R. Posner, K. Lill, J. H. W. de Wit, J. M. C. Mol and H. Terryn, Influence of surface hydroxyls on the formation of Zr-based conversion coatings on AA6014 aluminum alloy, *Surf. Coat. Technol.*, 2014, **254**, 277.

48 M. Bendova, J. Kolar, M. Marik, T. Lednicky and A. Mozalev, Influence of nitrogen species on the porous-alumina-assisted growth of $TiO_2$ nanocolumn arrays, *Electrochim. Acta*, 2018, **281**, 796.

49 G. K. Wertheim, F. J. DiSalvo and D. N. E. Buchanan, Site inequivalence in $Fe_{1+x}Nb_{3-x}Se10$, *Phys. Rev. B: Condens. Matter Mater. Phys.*, 1983, **28**, 3335.

50 X-ray photoelectron spectroscopy (XPS) reference pages, Selenium. **https://www.xpsfitting.com/search/label/Selenium** (accessed 2-May-2024).

51 N. Chubar, XPS determined mechanism of selenite ($HSeO_3^{2-}$) sorption in absence/presence of sulfate ($SO_4^{2-}$) on Mg-Al-$CO_3$ layered double hydroxides (LDHs): solid phase speciation focus, *J. Environ. Chem. Eng.*, 2023, **11**, 109669.

52 K. Shimizu, K. Kobayashi, P. Skeldon, G. E. Thompson and G. C. Wood, Anodic oxidation of zirconium covered with a thin layer of aluminium, *Thin Solid Films*, 1997, **295**, 156.

53 J. P. S. Pringle, The anodic oxidation of superimposed metallic layers: theory, *Electrochim. Acta*, 1980, **25**, 1423.

54 A. Mozalev, V. Khatko, C. Bittencourt, A. W. Hassel, G. Gorokh, E. Llobet and X. Correig, Nanostructured columnlike tungsten oxide film by anodizing Al/W/Ti layers on Si, *Chem. Mater.*, 2008, **20**, 6482.

55 C. Fernández-González, S. Ruiz-Gómez, A. Arché-Núñez, L. Pérez and C. Tavares de Sousa, Nano-patterning using ultra-thin alumina membranes, *Mater. Today Nano*, 2024, 100553, DOI: **10.1016/j.mtnano.2024.100553**.

56 A. Mozalev, A. J. Smith, S. Borodin, A. Plihauka, A. W. Hassel, M. Sakairi and H. Takahashi, Growth of multioxide planar film with the nanoscale inner structure via anodizing Al/Ta layers on Si, *Electrochim. Acta*, 2009, **54**, 935.

57 M. Bendova, J. Kolar, F. Gispert-Guirado and A. Mozalev, Porous-alumina-assisted growth of nanostructured anodic films on Ti−Nb alloys, *ChemElectroChem*, 2018, **5**, 2825.

58 Y. Kim, K. Yuan, B. R. Ellis and U. Becker, Redox reactions of selenium as catalyzed by magnetite: lessons learned from using electrochemistry and spectroscopic methods, *Geochim. Cosmochim. Acta*, 2017, **19**, 304.

59 W. M. Haynes, *CRC Handbook of Chemistry and Physics*, CRC Press, 2016.

60 K. Baek, N. Kasem, A. Ciblak, D. Vesper, I. Padilla and A. N. Alshawabkeh, Electrochemical removal of selenate from aqueous solutions, *Chem. Eng. J.*, 2013, **215**, 678.

61 X. Zhu and X. J. Loh, Layer-by-layer assemblies for antibacterial applications, *Biomater. Sci.*, 2015, **3**, 1505.

62 A. W. S. Dharmayanti, R. Dubey, N. K. Dubey and W.-P. Deng, Chapter 26 – Implant surface modification strategies through antibacterial and bioactive components, *Biopolym.-Based Formulations*, 2020, 647.

63 A. D'Agostino, F. Tana, A. Ettorre, M. Pavarini, A. Serafini, A. Cochis, A. C. Scalia, L. Rimondini, E. De Giglio and

 

S. Cometa, Mesoporous zirconia surfaces with anti-biofilm properties for dental implants, *Biomed. Mater.*, 2021, **16**, 045016.

64 Z. Fohlerova and A. Mozalev, Anodic formation and biomedical properties of hafnium-oxide nanofilms, *J. Mater. Chem. B*, 2019, **7**, 2300.

65 A. Mai-Prochnow, M. Clauson, J. Hong and A. B. Murphy, Gram positive and Gram negative bacteria differ in their sensitivity to cold plasma, *Sci. Rep.*, 2016, **6**, 38610.

66 D. P. Linklater, S. Saita, T. Murata, T. Yanagishita, C. Dekiwadia, R. J. Crawford, H. Masuda, H. Kusaka and E. P. Ivanova, Nanopillar polymer films as antibacterial packaging materials, *ACS Appl. Nano Mater.*, 2022, **5**, 2578.

67 J. Pekarkova, I. Gablech, T. Fialova, O. Bilek and Z. Fohlerova, Modifications of parylene by microstructures and selenium nanoparticles: evaluation of bacterial and mesenchymal stem cell viability, *Front. Bioeng. Biotechnol.*, 2021, **9**, 782799.

68 T. E. Catley, R. M. Corrigan and A. J. Parnell, Designing effective antimicrobial nanostructured surfaces: highlighting the lack of consensus in the literature, *ACS Omega*, 2023, **8**, 14873.

69 S. G. Higgins, M. Becce, A. Belessiotis-Richards, H. Seong, J. E. Sero and M. M. Stevens, High-aspect-ratio nanostructured surfaces as biological metamaterials, *Adv. Mater.*, 2020, **32**, 1903862.

70 S. W. M. A. I. Senevirathne, J. Hasan, A. Mathew, W. Woodruff and P. K. D. V. Yarlagadda, Bactericidal efficiency of micro- and nanostructured surfaces: a critical perspective, *RSC Adv.*, 2021, **11**, 1883.

71 T. Liu, Q. Cui, Q. Wu, X. Li, K. Song, D. Ge and S. Guan, Mechanism study of bacteria killed on nanostructures, *J. Phys. Chem. B*, 2019, **123**, 8686.

72 M. N. Dickson, E. I. Liang, L. A. Rodriguez, N. Vollereaux and A. F. Yee, Nanopatterned polymer surfaces with bactericidal properties, *Biointerphases*, 2015, **10**, 021010.

73 S. M. Kellher, O. Habimana, J. Lawler, B. O'Reilly, S. Daniels, E. Casey and A. Cowley, Cicada wing surface topography: An investigation into the bactericidal properties of nanostructural features, *ACS Appl. Mater. Interfaces*, 2016, **8**, 14966.

74 C. M. Bhadra, M. Werner, V. A. Baulin, V. K. Truong, M. A. Kobaisi, S. H. Nguyen, A. Balcytis, S. Juodkazis, J. Y. Wang, D. E. Mainwaring, R. J. Crawford and E. P. Ivanova, Subtle variations in surface properties of black silicon surfaces influence the degree of bactericidal efficiency, *Nano-Micro Lett.*, 2018, **10**, 36.

75 Y. Li, X. Ma, J. Zhang, X. Pan, N. Li, G. Chen and J. Zhu, Degradable selenium-containing polymers for low cytotoxic antibacterial materials, *ACS Macro Lett.*, 2022, **11**, 1349.

76 T. Huang, J. A. Holden, D. E. Heath, N. M. O'Brien-Simpson and A. J. O'Connor, Engineering highly effective antimicrobial selenium nanoparticles through control of particle size, *Nanoscale*, 2019, **11**, 14937.

77 D. M. Ridha, M. J. Al-Awady, A. J. A. Al-Zwaid, A. A. Balakit, H. O. M. Al-Dahmashi, M. H. Alataibi and G. A. El-Hiti, Antibacterial and antibiofilm activities of selenium nanoparticles-antibiotic conjugates against anti-multidrug-resistant bacteria, *Int. J. Pharm.*, 2024, **658**, 124214.

78 S. Wu, F. Zuber, K. Maniura-Weber, J. Brugger and Q. Ren, Nanostructured surface topographies have an effect on bactericidal activity, *J. Nanobiotechnol.*, 2018, **16**, 20.

79 M. Michalska, R. Divan, P. Noirot and P. D. Laible, Antimicrobial properties of nanostructured surfaces – demonstrating the need for a standard testing methodology, *Nanoscale*, 2021, **13**, 17603.

80 S. Wu, F. Zuber, J. Brugger, K. Maniura-Weber and Q. Ren, Antibacterial Au nanostructured surfaces, *Nanoscale*, 2016, **8**, 2620.

81 E. P. Ivanova, D. P. Linklater, M. Werner, V. A. Baulin, X. Xu, N. Vrancken, S. Rubanov, E. Hanssen, J. Wandiyanto, V. K. Truong, A. Elbourne, S. Maclaughlin, S. Juodkazis and R. J. Crawford, The multi-faceted mechano-bactericidal mechanism of nanostructured surfaces, *Proc. Natl. Acad. Sci. U. S. A.*, 2020, **117**, 12598.

82 M. Ganjian, L. Angeloni, M. J. Mirzaali, K. Modaresifar, C. W. Hagen, M. K. Ghatkesar, P.-L. Hagedoorn, L. E. Fratila-Apachitei and A. A. Zadpoor, Quantitative mechanics of 3D printed nanopillars interacting with bacterial cells, *Nanoscale*, 2020, **12**, 21988.

83 Q. Cui, T. Liu, X. Li, K. Song and D. Ge, Nanopillared polycarbonate surfaces having variable feature parameters as bactericidal coatings, *ACS Appl. Nano Mater.*, 2020, **3**(5), 4599.